Journal of Molecular Modeling (2021) 27:320
https://doi.org/10.1007/s00894-021-04917-8

ORIGINAL PAPER

On the formation of CN bonds in Titan's atmosphere—a unified reaction valley approach study

Marek Freindorf[1] · Nassim Beiranvand[1] · Alexis A. A. Delgado[1] · Yunwen Tao[1] · Elfi Kraka[1]

Received: 1 July 2021 / Accepted: 15 September 2021

Abstract

In this work, we investigated the formation of protonated hydrogen cyanide $HCNH^+$ and methylene amine cation $CH_2NH_2^+$ (both identified in Titan's upper atmosphere) from three different pathways which stem from the interaction between CH_4 and $N^+(^3P)$. As a mechanistic tool, we used the Unified Reaction Valley Approach (URVA) complemented with the Local Mode Analysis (LMA) assessing the strength of the CN bonds formed in these reactions. Our URVA studies could provide a comprehensive overview on bond formation/cleavage processes relevant to the specific mechanism of eight reactions **R1**–**R8** that occur across the three pathways. In addition, we could explain the formation of $CH_2NH_2^+$ and the appearance of $HCNH^+$ and $CHNH_2^+$ along these paths. Although only smaller molecules are involved in these reactions including isomerization, hydrogen atom abstraction, and hydrogen molecule capture, we found a number of interesting features, such as *roaming* in reaction **R3** or the primary interaction of H_2 with the carbon atom in $HCNH^+$ in reaction **R8** followed by migration of one of the H_2 hydrogen atoms to the nitrogen which is more cost effective than breaking the HH bond first; a feature often found in catalysis. In all cases, charge transfer between carbon and nitrogen could be identified as a driving force for the CN bond formation. As revealed by LMA, the CN bonds formed in reactions **R1**–**R8** cover a broad bond strength range from very weak to very strong, with the CN bond in protonated hydrogen cyanide $HCNH^+$ identified as the strongest of all molecules investigated in this work. Our study demonstrates the large potential of both URVA and LMA to shed new light into these extraterrestrial reactions to help better understand prebiotic processes as well as develop guidelines for future investigations involving areas of complex interstellar chemistry. In particular, the formation of CN bonds as a precursor to the extraterrestrial formation of amino acids will be the focus of future investigations.

Keywords Vibrational spectroscopy · Unified reaction valley approach · Local mode analysis · Titan · Formation of extraterrestrial CN bonds

Marek Freindorf and Nassim Beiranvand contributed equally to this work.

This article belongs to the Topical Collection: *VIII Symposium on Electronic Structure and Molecular Dynamics – VIII SeedMol*

✉ Elfi Kraka
ekraka@smu.edu

Marek Freindorf
mfreindorf@smu.edu

Nassim Beiranvand
nbeiranvand@smu.edu

Alexis A. A. Delgado
aadelgado@smu.edu

Yunwen Tao
yunwent@smu.edu

[1] Chemistry Department, SMU, Fondren Science Building, Dallas, 75275-0314, TX, USA

Introduction

At least 200 specific molecular constituents including neutral molecules and charged species have been identified so far in the interstellar medium (ISM) [1–5]. The number is constantly increasing because of advanced detection techniques onboard space crafts such as the *Cassini* [6, 7], and space-based and terrestrial telescopes (ranging from the Spitzer Space Telescope [8], Hubble Space Telescope [9], the James Webb Telescopes [10], to the planned Giant Magellan Telescope [11] (just to name a few)), being complemented with sophisticated terrestrial experimental investigations [12–14]. The interstellar chemistry involving these species, which is often triggered by intense UV light, has recently attracted a lot of attention [15–19]. One area of interest pertains to the formation of organic aerosols (tholins) [20], as such molecules have been considered possible prebiotic precursors of nucleic acids, proteins, amino sugars, and other compounds [17, 21–23]. It is

Published online: 11 October 2021

assumed that early earth was a tholin-rich place [24] with thiolin-like materials having been found on Saturn's largest moon, Titan [4, 25–27], Neptune's largest moon, Triton [20], and on smaller icy bodies [12, 28].

Titan's dense atmosphere consists primarily of N_2 and a small percentage of CH_4 [29] which have been presumed to have formed thiolins. In Titan's upper atmosphere, Cassini's Ion and Neutral Mass Spectrometer (INMS) detected neutral and positive ion signatures [30] primarily for protonated hydrogen cyanide (i.e., $HCNH^+$, iminomethyl cation) [31, 32], the methylene amine cation (i.e, $CH_2NH_2{}^+$) [33–35], the methanimine cation (i.e., CH_2NH^+), and its isomer the aminomethylene cation (i.e., $CHNH_2^+$) [36]. A key component for the formation of $HCNH^+$ has been attributed to the ionic dissociation of N_2 into $N^+(^3P)$ via extreme ultraviolet radiation [15], ions, and energetic electrons [31, 32]. High-pressure mass spectrometry experiments, in combination with computational studies, have revealed that $N^+(^3P)$ reacts with CH_4 to form $HCNH^+$ [37]. However, the formation of $CH_2NH_2^+$ and the appearance of $HCNH^+$ and $CHNH_2^+$ along this path have yet to be comprehensively understood.

From the reaction between CH_4 (**1**) and $N^+(^3P)$ (**2**), three different pathways for the synthesis of $HCNH^+$ (**7**) and CH_2NH_2 (**4S**) result (see Fig. 1). In this work, we investigate these three pathways. *Path 1* includes the reactions **R2**, **R3**, **R4**, and **R8**; *path 2* includes reactions **R5**, **R6**, and **R8**. In addition to these two paths, we also consider *path 3* which starts from the singlet state of CH_3NH^+ (**3S**), resulting from intersystem crossing of the triplet state CH_3NH^+ (**3T**), and includes reactions **R7** and **R8**. The main focus of this study is to explore the detailed mechanism of the formation of $HCNH^+$ (**7**) and $CH_2NH_2{}^+$ (**4S**) using the Unified Reaction Valley Approach (URVA) [38] and to quantitatively assess and compare the strength of the CN bonds formed in these reactions through local vibrational mode analysis [39]. Our results will give new insights into these extraterrestrial reactions to help better understand prebiotic processes as well as develop guidelines for future investigations involving areas of complex interstellar chemistry.

Computational methods

The main tool applied in this work is URVA [38, 40, 41]. A comprehensive review can be found in Ref. [38]; therefore, in the following, only the key essentials will be summarized. URVA analyses the curvature of the reaction path traced out by the reaction complex (i.e., the union of reacting molecules) on the potential energy surface (PES) moving from the entrance channel up to the transition state (TS), from here, down into the product channel. Any electronic structure changes including bond breaking/forming processes, re-hybridization, charge polarization and transfer, etc., lead to distinct curvature peaks which are directly reflected in the scalar reaction path curvature calculated at each path point, whereas regions of minimal electronic change are reflected by curvature minima where the region from one curvature minimum to

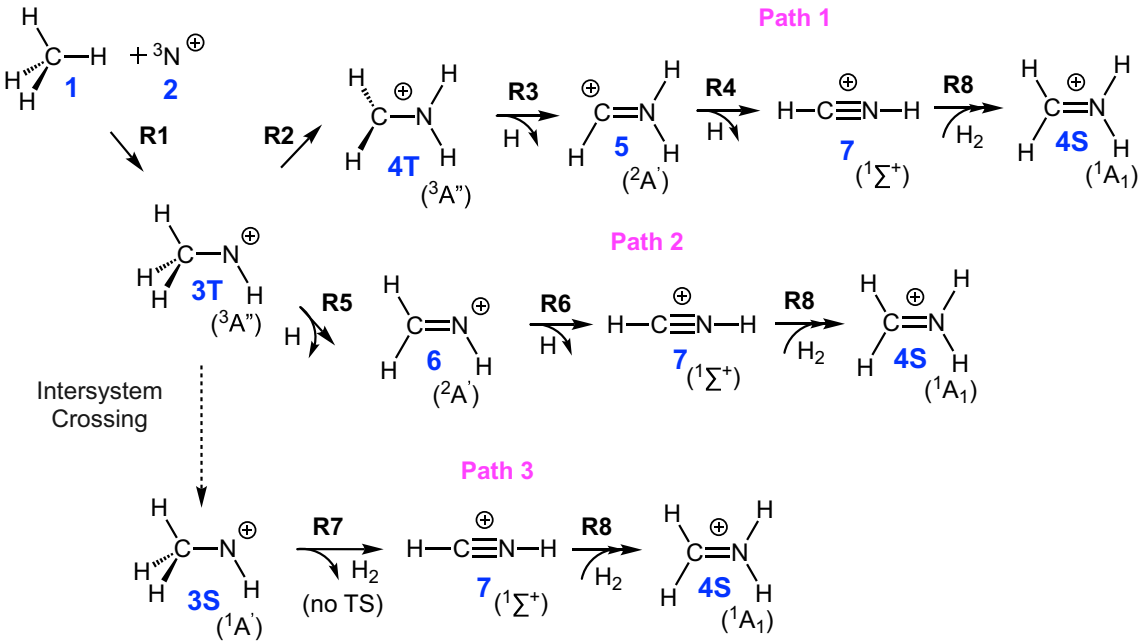

Fig. 1 Reaction pathways investigated in this work

the next embedding a curvature peak is called a reaction phase. Each chemical reaction has a unique pattern of curvature maxima and minima with a different number of reaction phases, which can be used as its characteristic *fingerprint* [38]. We then decompose the reaction curvature along the reaction path into individual components such as bond lengths, bond angles, and dihedral angles or puckering coordinates to get a deeper understanding of each chemical event [40]. The sign of a component indicates if the parameter in question supports the chemical event (positive sign) or if it resists the chemical change (negative sign) [40]. For a detailed mathematical derivation and recent advances of URVA, interested readers are referred to Ref. [38].

Another important tool used for the assessment of the CN bond strength in molecules **3**–**7** and TSs **TS1**–**TS6** and **TS8** of the corresponding reactions **R1**–**R6** and **R8** investigated in this work is the local vibrational mode analysis (LMA). A comprehensive review of the underlying theory can be found in Ref. [39]. Therefore, in the following, only some essentials are summarized. Normal vibrational modes are generally delocalized as a result of kinematic and electronic coupling [42–44]. In other words, if one considers a particular normal stretching mode between two atoms of interest, it can be coupled to other normal modes such as bending or torsion, which inhibits the direct correlation between stretching frequency and bond strength as well as the comparison between stretching modes in related molecules. As a consequence, the normal stretching force constant cannot be used as a direct bond strength measure. One needs to derive local counterparts that are free from any mode-mode coupling. Konkoli, Cremer, and co-workers solved this problem by solving the mass-decoupled analogue of Wilson's equation of vibrational spectroscopy [45–49] leading to local vibrational modes, associated local mode frequencies, and local mode force constants. Zou and Cremer showed that the local stretching force constant k^a reflects the curvature of the PES in the direction of the bond stretching [50]. This important result qualifies the local stretching force constants k^a as unique quantitative measures of the intrinsic strength of chemical bonds and/or weak chemical interactions based on vibrational spectroscopy, which has been extensively applied in previous work as documented in Ref. [39]. For some more recent works, see also Refs. [51–57].

Geometry optimizations and frequency calculations including a local mode analysis for all stationary points (i.e., reactants, products, and TSs) of each reaction **R1**–**R8** were performed with second Møller-Plesset perturbation theory (MP2) [58, 59] and complete active space perturbation theory of second order (CASPT2) [60–62] using Dunning's aug-cc-pVTZ basis set [63] as well as with Coupled Cluster theory [64–66] at the CCSD(T) level [67–69] using Dunning's cc-pVDZ basis set [63]. The active space in the CASPT2 calculations included 4-electrons with 4-orbitals, 5-electrons with 5-orbitals, and 6-electrons with 6-orbitals, depending on the molecular system. For the reaction path calculations and URVA analysis, MP2/aug-cc-pVTZ was applied. For the reaction path, the intrinsic reaction coordinate (IRC) of Fukui [70] was used with a step size of $s = 0.03$ amu$^{1/2}$ Bohr, applying the improved reaction path following the algorithm of Hratchian and Kraka, enables one to follow a chemical reaction far out into entrance and exit channel [71]. All IRC calculations were performed with the Gaussian16 program package [72] at the MP2/aug-cc-pTZ level of theory using a tight convergence criterion. The CASPT2 calculations were performed with MOLPRO [73–75]. For the CCSD(T) calculations, the CFOUR program package [66] was utilized. The URVA analysis was carried out with the program pURVA [76] and the local mode analysis with the program LModeA [77]. The computation and analysis of atomic charges were done with the NBO program of Weinhold and co-workers [78–80].

Results and discussion

In the following, the energetics of reactions **R1**–**R8**, their specific mechanism as revealed by URVA, and the bond strength of all CN bonds formed during these reactions via local vibrational force constants will be discussed. In addition to tables and figures presented in the manuscript, further information on geometries, NBO charges, and reaction movies are collected in the Supporting Information.

Energetics results

Table 1 presents activation energies E^a, activation enthalpies H^a, and activation free energies G^a, as well as reaction energies E_r, reaction enthalpies H_r, and reaction free energies G_r, calculated with CASPT2/aug-cc-pVTZ and CCSD(T)/cc-pVDZ model chemistries. The corresponding MP2/aug-cc-pVTZ results can be found in the Supporting Information. The energetics presented in Table 1 were calculated in each case relative to the reactant of the corresponding reaction. Although both model chemistries have a different focal point, i.e., CASPT2 on multireference character [81] and CCSD(T) on dynamic correlation [64–66], results are quite similar, confirming that both approaches lead to a reliable description of reactions **R1**–**R8**. The following discussion is limited to the CCSD(T) results.

Reaction **R1** starts from an intermediate (as shown in Fig. 2a) which is formed directly from methane (**1**) and $N^+(^3P)$ (**2**) in a barrier less, strongly exothermic reaction with a reaction energy of −88.34 kcal/mol. From the intermediate, the product **3T** is formed with

Table 1 Activation energies E^a, enthalpies H^a, and free energies G^a; reaction energies E_r, enthalpies H_r, and free energies G_r (kcal/mol) of the reactions **R1**–**R8** investigated in our study. Optimal geometries and frequencies calculated at the CASPT2/aug-cc-pVTZ and CCSD(T)/cc-pVDZ levels of theory

	CASPT2/aug-cc-pVTZ						CCSD(T)/cc-pVDZ					
Reaction	E^a	E_r	H^a	H_r	G^a	G_r	E^a	E_r	H^a	H_r	G^a	G_r
R1[1]	1.62	−68.5	0.72	−66.83	0.62	−66.57	3.78	−66.14	1.97	−64.64	3.08	−63.95
R2	42.62	−7.82	39.42	−7.46	40.13	−7.49	46.12	−4.31	42.89	−3.91	43.53	−3.51
R3	42.50	40.09	38.58	36.10	39.07	29.46	41.20	37.39	37.19	31.56	37.35	26.26
R4	49.55	38.69	42.97	32.35	42.56	26.07	50.93	37.84	44.46	31.56	44.06	25.27
R5	39.50	39.24	34.16	33.84	34.26	27.00	40.86	38.61	35.6	33.29	35.73	26.50
R6	35.48	31.72	30.51	27.15	30.09	21.05	38.14	32.21	33.26	27.61	32.87	21.48
R7	–	−72.53	–	−74.00	–	−81.37	–	−67.94	–	−71.61	–	−73.24
R8	42.23	−54.86	45.64	−46.02	53.16	−38.35	39.60	−55.87	43.18	−47.14	50.70	−39.50

[1] Values relative to the intermediate

a small activation energy of only 3.78 kcal/mol. The reaction energy with −66.14 kcal/mol indicates the strong exothermic character of **R1**. In summary, the formation of **3T** from **1** and **2** leads to an overall energy gain of 155 kcal/mol; this large amount of excess energy facilitates all following reactions and counterbalances activation energies

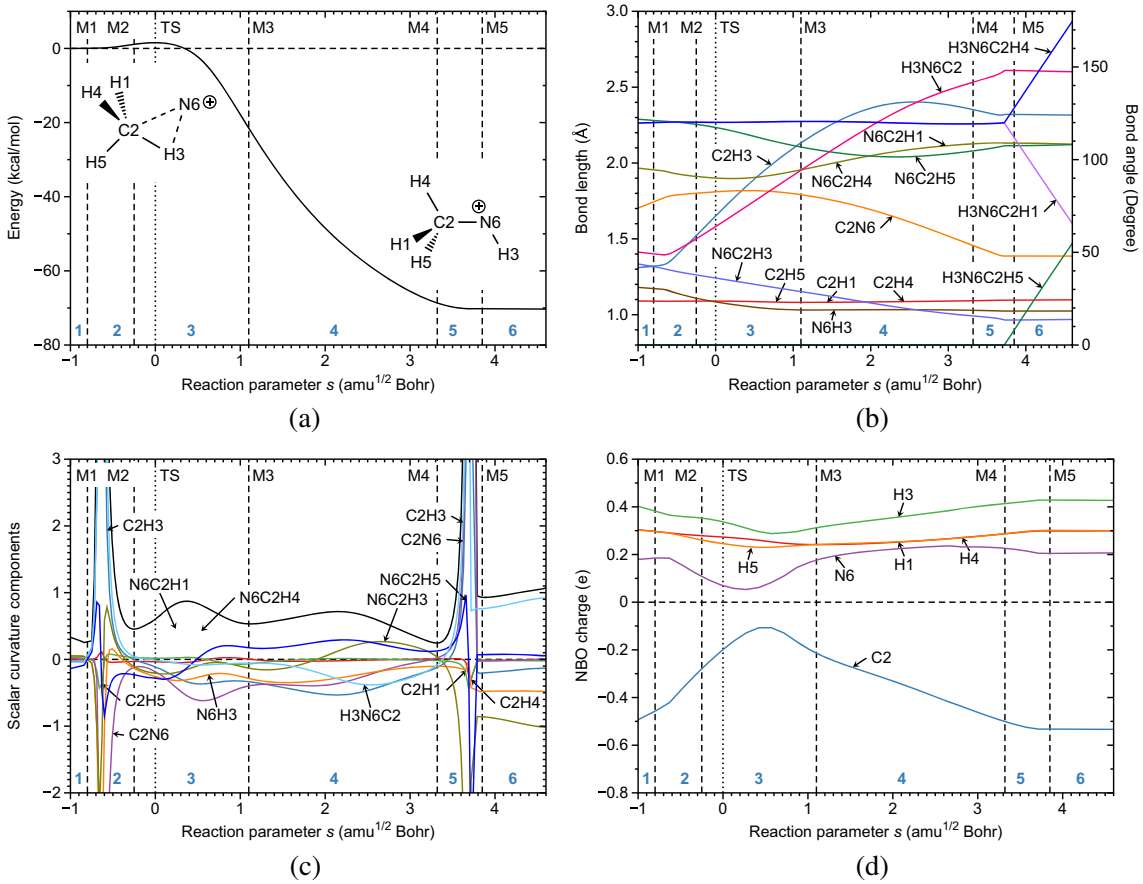

Fig. 2 Reaction **R1**; **a** energy profile; **b** changes in geometry parameters, **c** reaction path curvature profile (black solid line) and its decomposition into components, **d** changes in NBO charges as a function of the reaction path parameter s. Reaction phases are indicated by vertical dashed lines at curvature minima M1, M2, ..., Mn, and are labeled by blue numbers. The TS is indicated as a dotted line. MP2/aug-cc-pVTZ level of theory

in the range of 40–50 kcal/mol as found for **R2**–**R6** and **R8**.

As shown in Fig. 1, **3T** serves as a reactant for three different pathways, which start either on a triplet (*path 1* and *path 2*) or directly on a singlet potential energy surface (PES) after intersystem crossing (*path 3*). Reaction **R2** is the first reaction of *path 1* where **3T** undergoes isomerization to **4T** with an activation energy of 46.12 kcal/mol, and a reaction energy of −4.31 kcal/mol. By losing a hydrogen atom **4T** transforms in reaction **R3** into **5** with an activation and reaction energy of 41.20 and 37.39 kcal/mol, respectively, i.e., this reaction is strongly endothermic. The next step of this pathway is reaction **R4**, in which **5** loses another H atom transforming into **7** with an activation and reaction energy of 50.93 and 37.84 kcal/mol, respectively, revealing again the strong endothermic character of this reaction.

The alternative *path 2*, starting from **3T**, proceeds directly to losing a hydrogen atom and transforming into **6** in reaction ***R5***. The activation and the reaction energies are 40.86 and 38.14 kcal/mol, respectively, comparable with the energetics found for reaction **R3**. The next step along *path 2* is reaction **R6**, where the loss of another hydrogen atom from **6** leads to **7**, with the activation and reaction energy values of 38.61 and 32.21 kcal/mol. Comparing the number of reactions in both pathways, the cumulative activation energies, and endothermicities, *path 2* seems to be more favorable.

In contrast to *path 1* and *path 2*, *path 3* starts on a singlet PES. **3T** undergoes intersystem crossing forming **3S**. However, **3S** is unstable (ST splitting: 35.59 kcal/mol) and transforms directly into **7** via H_2 abstraction in barrierless reaction **R7** with a reaction energy –67.94 kcal/mol, definitely favoring *path 3* as the most likely path.

Protonated hydrogen cyanide **7**, one of the key species found in Titan's atmosphere being formed in all three pathways, can then transform into the methylene amine cation **4S**, another key species in Titan's atmosphere via the addition of H_2 in reaction **R8**. The activation and the reaction energies are 39.60 and −55.87 kcal/mol, respectively, revealing the strong exothermic character of this chemical transformation. Whereas the discussion of the energetics provides valuable overall trends, it cannot lead to specific insights into the actual reaction mechanism, due to the nature of the energy being a cumulative property [82–87]. Therefore, in the following, a detailed mechanistic study will be presented based on URVA.

Reaction mechanisms

The mechanism of each of the reactions **R1**–**R8** will be described in detail, in particular in terms of the energy profiles, curvature profiles, and their decomposition as well as changes of important geometry parameters and changes of the NBO charges monitoring charge transfer along the reaction parameter s. The decomposition of the reaction path direction along the reaction parameter s for each reaction can be found in the Supporting Information. In addition, reaction movies following the changes of the reaction complex along the reaction parameter s for each of the reactions are included in the Supporting Information, facilitating the discussions.

Reaction **R1** describes the isomerization of the intermediate originally formed from **1** and **2** to methylamino radical cation **3T**. As shown in Fig. 2a in the intermediate the migrating methyl hydrogen atom H3 is in a bridging position between carbon atom C2 and nitrogen atom N6 (R(C2N6) = 1.693 Å, R(C2H3 = 1.308 Å, R(N6H3) = 1.183 Å. During the reaction (see reaction movie **SR1**, Supporting Information), H3 swings around to the nitrogen atom, the C2H3 bond is cleaved, and the new C2N6 and N6H3 bonds are formed. Furthermore, the molecules rotate from an eclipsed into a more stable staggered conformation. Figure 2b shows the changes of the most relevant geometry parameters along with the reaction parameter s. It is interesting to note that the distance of the C2N6 bond to be formed first increases, reaching a maximum value of 1.818 Å at s= 0.4 amu$^{1/2}$ Bohr, i.e., shortly after the TS before decreasing to its final value of 1.386 Å at s= 3.7 amu$^{1/2}$ Bohr. Another interesting feature of the reaction is the rotation from an eclipsed into the staggered form starting at s= 3.8 amu$^{1/2}$ Bohr and being completed at the end of the reaction path at s= 4.7 amu$^{1/2}$ Bohr. Figure 2b shows the corresponding reaction profile. As expected from the small barrier, the entrance channel is relatively short (stretching only over 1 path unit) compared to the exit channel of this strongly exothermic reaction (stretching over almost 5 path units). Figure 2c shows the scalar curvature along s, resulting in 5 curvature minima, which divide the reaction path into 6 reaction phases with phase 3 containing the TS. Only chemical events before the TS account for the reaction barrier, i.e., the large curvature peak in phase 2 is composed of the events determining the barrier which are further characterized by decomposition of the reaction path curvature into components. The cleavage of the already weakened C2H3 bond starts here, characterized by supportive contributions (positive values) of the C2H3 bond length and N6C2H3 angle, whereas the formation of the new C2N6 and N3H3 bonds is resisting (negative values). Interesting to note is that there is no pronounced peak at the TS, in accordance with our frequent findings that important chemical changes do not necessarily occur at the TS, they may occur in the entrance [88, 89] or exit channel of a reaction [40, 90]. The smaller curvature peaks in phases 3 and 4 are dominated by CNH angle contributions describing the migration of the

H3 atom accompanied with the bond breaking/forming processes. The large curvature peak in phase 5 far out in the exit channel characterizes the simultaneous finalization of the C2H3 bond breaking and C2N6 and N6H3 bond formation events, accompanied by the rotation of the molecule into the final staggered conformation. Stretching over the whole reaction rather than occurring in an abrupt fashion is more energy conserving, a phenomenon which we also have frequently observed for other chemical reactions, in particular catalysis reactions [91, 92]. Changes of the NBO charges as a function of s, reflecting charge-transfer, are shown in Fig. 2d. At the beginning and at the end of the reaction, the N atoms have a positive charge of $0.2e$, i.e., the remaining $0.8e$ are distributed over the methyl group, the carbon atom has a negative charge of $-0.5e$ (compared to $-0.7e$ in methane), each of the spectator hydrogen atoms has a positive charge of $0.3e$ (compared to $0.18e$ in methane), and the migrating H atom has the largest positive charge of $0.4e$. Whereas the charges on the H-atoms remain fairly constant during the course of the reaction, there is a transfer of negative charge from the C to the N atom with a maximum reached at s= 0.4 amu$^{1/2}$ Bohr (charge on C2: $-0.1e$ and on N6: $0.3e$ with Δ(NBO) = $0.4e$ compared to Δ(NBO) = $0.7e$ at the start). This weakens the electrostatic interaction between the two atoms. s = 0.420 amu$^{1/2}$ Bohr is also the point where the maximum CN distance is reached. After that point, negative charge is transferred back to the C atom, Δ(NBO) and with that the bond polarity increases again supporting the formation of the CN bond. Figure 1 depicts the central role of the methylamino radical cation **3T** which serves as a starting point for each of the following 3 pathways leading to the formation of protonated hydrogen cyanide HCNH$^+$ **7**; *path 1* with reactions **R2**–**R4**, *path 2* with reactions **R5** and **R6**, and *path 3* with reaction **R7**.

Reaction **R2** describes the isomerization of the methylamino cation **3T** to the methylene amino cation **4T**. The reaction is only slightly exothermic by about 6 kcal/mol leading to entrance and exit channels of about the same lengths (2.3 amu$^{1/2}$ Bohr). During this reaction, the H4 atom of the methyl group migrates from the C3 to the N2 atom, the C3H4 bond is cleaved, and a new N2H4 bond is formed (see Fig. 3a and reaction movie **SR2**, Supporting Information). The carbon atom changes from sp^3 to sp^2 hybridization. However, since the methyl and amino hydrogen atoms of the resulting **4T** are arranged almost perpendicular to each other (H1N2C3H5=81°), the formation of a CN double bond is not possible. As shown in Fig. 3b, the CN bond distance remains fairly constant during the whole reaction (1.386 Å in **3T** compared to 1.396 Å in **4T**), which corresponds to a typical CN single bond distance. Most changes are observed for the N2H4 distance starting from 2.025 Å in **3T** and reaching its final value of 1.031 Å at s= 1.1 amu$^{1/2}$ Bohr and the C3H4 distance, starting from 1.094 Å in **3T** and reaching its final value of 2.118 Å at the end of the reaction at s= 2.3 amu$^{1/2}$ Bohr. At **TS2**, the migrating hydrogen atom is in a bridging position, with a C3H4 distance of 1.358 Å, a N2H4 distance of 1.239 Å, and a C3N2H4 angle of 62°. Figure 3c presents the scalar reaction path curvature and its decomposition into components along s, which are characterized by six reaction phases. Interesting to note that also for this reaction, there is no significant curvature at the TS; major events occur in both entrance and exit channel. The large curvature peaks in phase 1 as well as in phase 6 are predominantly characterized by rotations of the methyl hydrogens H5 and H6 adjusting to the rehybridization, at the carbon atom. The cleavage of the C3H4 bond stretches over phases 3–5, starting with a small supporting contribution of the C3H4 component in phase 3, a small resisting contribution in phase 4, and a larger resisting contribution in phase 5 in which the C3H4 distance of 2.117 Å is reached as confirmed by Fig. 3b. With the breakage of the C3H4 bond, the new N2H4 bond starts to form, reaching the final distance of 1.023 Å already in phase 4. As reflected by the large curvature contributions shown in Fig. 3c, the H1N2C3 angle plays a central role for the reaction. Changing from 147° to 122° helps push the carbon hydrogens H5 and H6 into an sp^2 position and make room at the nitrogen for the incoming H4. This is also visualized in the reaction movie **SR2** of the Supporting Information. Figure 3d shows the changes of the NBO charges as a function of s. Starting in phase 2, there is a large transfer of negative charge from the C to the N atom. The original difference Δ(NBO) decreases from $0.74e$ to 0 at the TS, where both C and N have a negative charge of $-0.25e$. After that point, the negative charge of N is slightly increasing and that of the C atom is slightly decreasing to the final values of $-0.23e$ for N and $-0.13e$ for C in **4T**, where the positive charge is equally distributed among the hydrogen atoms (charges on H5 and H6 $0.25e$, respectively, and on H1 and H4 $0.43e$, respectively).

In reaction **R3**, the methylene amino cation **4T** loses one hydrogen atom at the carbon atom and transforms into the planar aminomethylene cation **5** with a CN double bond. C2H6 bond breakage is initiated by a rotation of both the carbon and nitrogen hydrogens from an almost perpendicular to planar arrangement plane (see Fig. 4a and reaction movie **SR3**, Supporting Information). As revealed by Fig. 4b, the largest geometry changes in the entrance channel include the dihedral angles H1C2N3H4 approaching 180° and H1C2N3H5 approaching 0° during the course of the reaction. At s= −1.5 amu$^{1/2}$ Bohr, the rotation has reached a critical point (H1C2N3H4= 138° and H1C2N3H5=50°) and the C2H6 bond starts to lengthen almost linearly. The C2N3 bond distances decrease from 1.396 Å in **4T** to its final value of 1.250Å at the path endpoint s= 2.0 amu$^{1/2}$ Bohr. Figure 4c shows the reaction path curvature which is composed of 6 reaction phases and

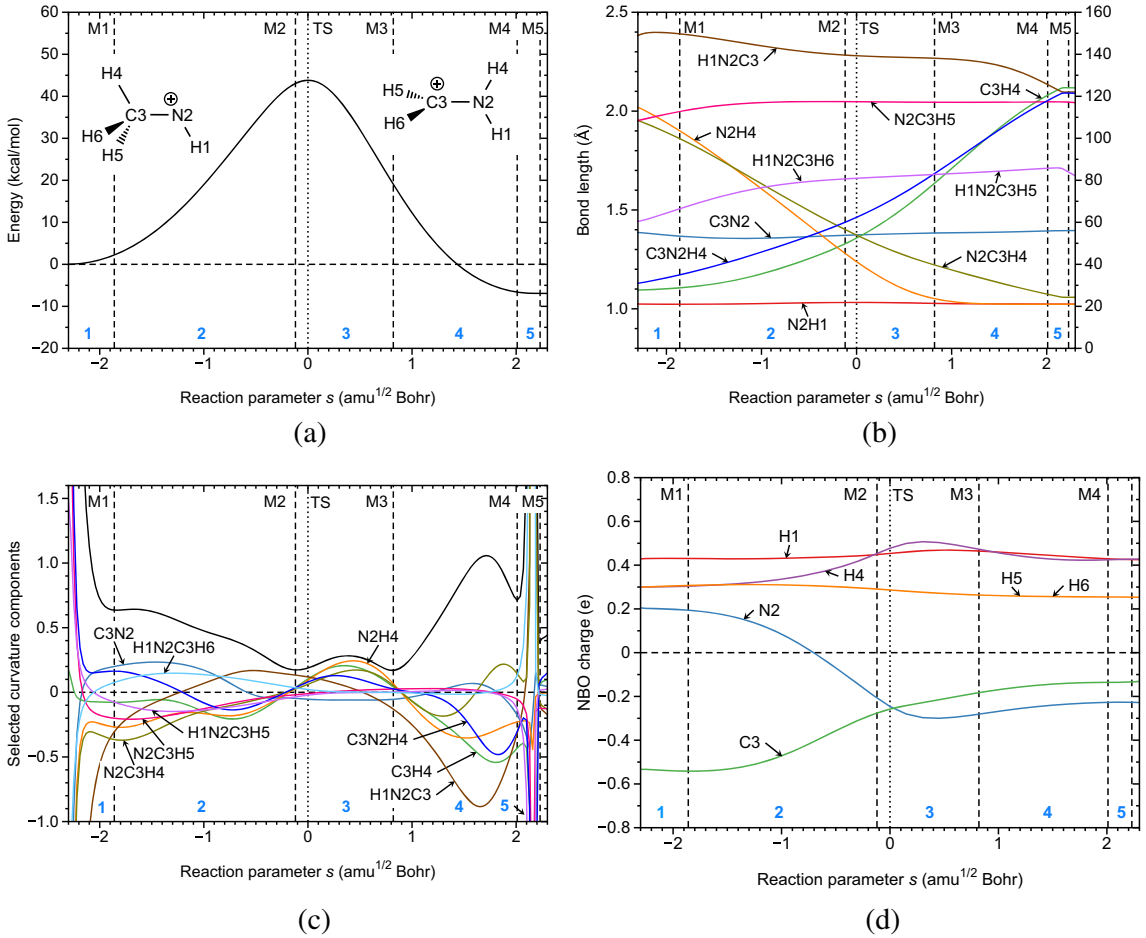

Fig. 3 Reaction **R2**; **a** energy profile; **b** changes in geometry parameters; **c** reaction path curvature profile (black solid line) and its decomposition into components; **d** changes in NBO charges as a function of the reaction path parameter s. Reaction phases are indicated by vertical dashed lines at curvature minima M1, M2, ..., Mn, and are labeled by blue numbers. The TS is indicated as a dotted line. MP2/aug-cc-pVTZ level of theory

its decomposition into components. The curvature peaks in phase 1 are characterized by methyl and amino hydrogen rotations which are complemented in phase 2 by changes of the H1C2N3 and at the end of this phase by changes of the H6C2N3 bond angle. In phase 3, the cleavage of the C2H6 bond takes place as indicated by a large supporting contribution of the C2H6 component with a smaller contribution from C2N3. The curvature maximum occurs at $s = -1.3$ amu$^{1/2}$ Bohr, where the C2H6 distance starts to increase (see Fig. 4b). In summary, the energy-demanding cleavage of a CH bond is assisted by methyl and amino hydrogen rotations guiding the CH_2 group in a position facilitating the bond breaking process. Phase 4 including **TS3** and phase 5 show only small curvature enhancements predominately made up from C2N3 bond adjustments and further hydrogen bond rotations. Phase 6 is dominated by final H6C2N3 changes and rotations about the CN bond needed to achieve the planar structure of resulting **5**. Figure 4d depicts changes of the NBO charges along s. Major changes occur for the carbon and nitrogen atoms. In phase 3, negative charge is transferred from C2 to N3 where at the end of phase 3 N3 almost reaches its final charge of $-0.7e$ and C2 adapts a positive charge of $0.25e$. In the following phases 4–6, i.e., to the end of the reaction, an additional negative charge is transferred from the C2 atom to the leaving H6 atom bringing its charge to 0, a small portion is also transferred to H1. At the end of the reaction with NBO charges of $-0.7e$ on N and $0.54e$ on C2, a strongly polar CN double bond results in **5**.

In reaction **R4**, the aminomethylene cation **5** loses an additional amino hydrogen atom leading to the protonated hydrogen cyanide **7**. In resemblance with reaction **R3**, here the NH bond breakage is assisted by rotating the C2H1 bond and the N3H4 bonds into a linear arrangement which facilitates the cleavage of the N3H5 bond (see Fig. 5a and reaction movie **SR4**, Supporting Information). The reaction movie also shows an interesting feature of this reaction. Hydrogen atom H5 orbits around the NH end

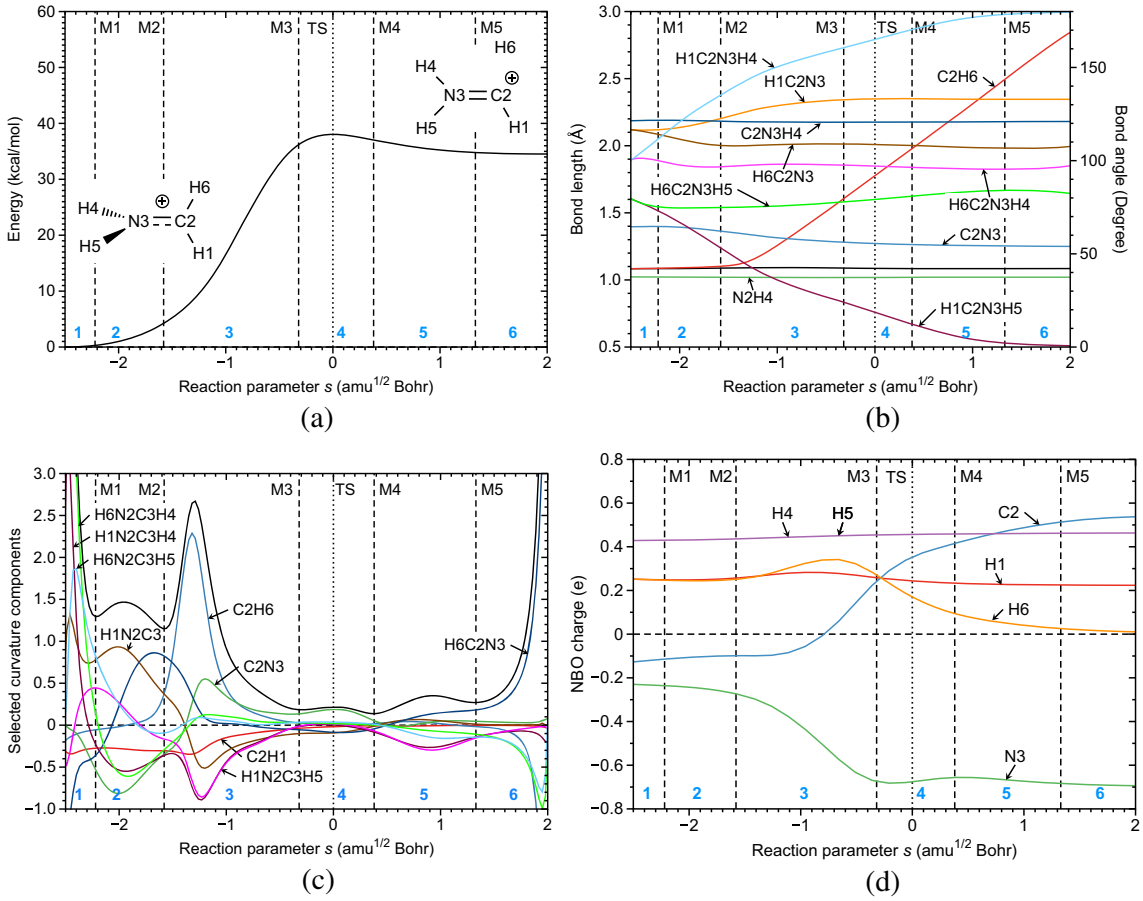

Fig. 4 Reaction **R3**; **a** energy profile; **b** changes in geometry parameters; **c** reaction path curvature profile (black solid line) and its decomposition into components; **d** changes in NBO charges as a function of the reaction path parameter s. Reaction phases are indicated by vertical dashed lines at curvature minima M1, M2, ..., Mn, and are labeled by blue numbers. The TS is indicated as a dotted line. MP2/aug-cc-pVTZ level of theory

instead of leaving on a more straight pathway (i.e., so-called *roaming*) which causes the long exit channel of almost eight s units. For a recent review on the phenomenon of roaming reactions, their experimental capture and potential importance of astrochemistry, see e.g. Refs. [93–95]. Figure 5b depicts changes of bond lengths and bond angles as a function of s. The H1C2N3 angles starts to widen from 133° in **5** with a steep incline until $s = -1.1$ amu$^{1/2}$ Bohr, where a value of 162° is reached. After that path point, the H1C2N3 angle slowly increases to its final value of 180°. Starting from a value of 121°, the C2N3H4 angle first moves through a shallow minimum, then steeply increases and reaches the value of 178° at s=2.0 amu$^{1/2}$ Bohr. The N3H5 bond length starts to linearly increase at $s = -1.2$ amu$^{1/2}$ Bohr until it reaches a maximum value of 3.111 Å at s=3.3 amu$^{1/2}$ Bohr, where the C2N3H5 angle adapts a value of 120°. From there on, the roaming of H5 starts, leading to a small decrease of the N3H5 distance to 2.896 Å and a steep incline of the C2N3H5 angle to its final value of 180°. The C2N3 bond decreases slightly in the entrance channel and shortly after **TS4** at s=0.5 amu$^{1/2}$ Bohr attains its final value of 1.144 Å corresponding to a typical CN triple bond. In addition to roaming, reaction **R4** has another interesting feature, more frequently observed in transition metal catalysis [96], the involvement of formation of a dihydrogen interaction [97, 98] in the reaction mechanism. The H4H5 distance first decreases to 1.687 Å at $s = -1.1$ amu$^{1/2}$ Bohr, the point where N3H5 bond breakage starts, adapts a maximum value of 2.767 Å at s=3.0 amu$^{1/2}$ Bohr, and then decreases again caused by the roaming motion of the H5 atom (see reaction movie **SR4**, Supporting Information). The reaction path curvature profile and its decomposition shown in Fig. 5c quantify these observations. The reaction is composed of seven distinct phases. Phase 1 is characterized by angle rotations, then in phase 2 the N3H5 bond starts to break, supported by H4H5 interactions leading to a large curvature peak. Another important contribution to this curvature peak is negative contribution of the H1C2N3 angle, resisting to become linear. The curvature peak in phase 3 shortly after

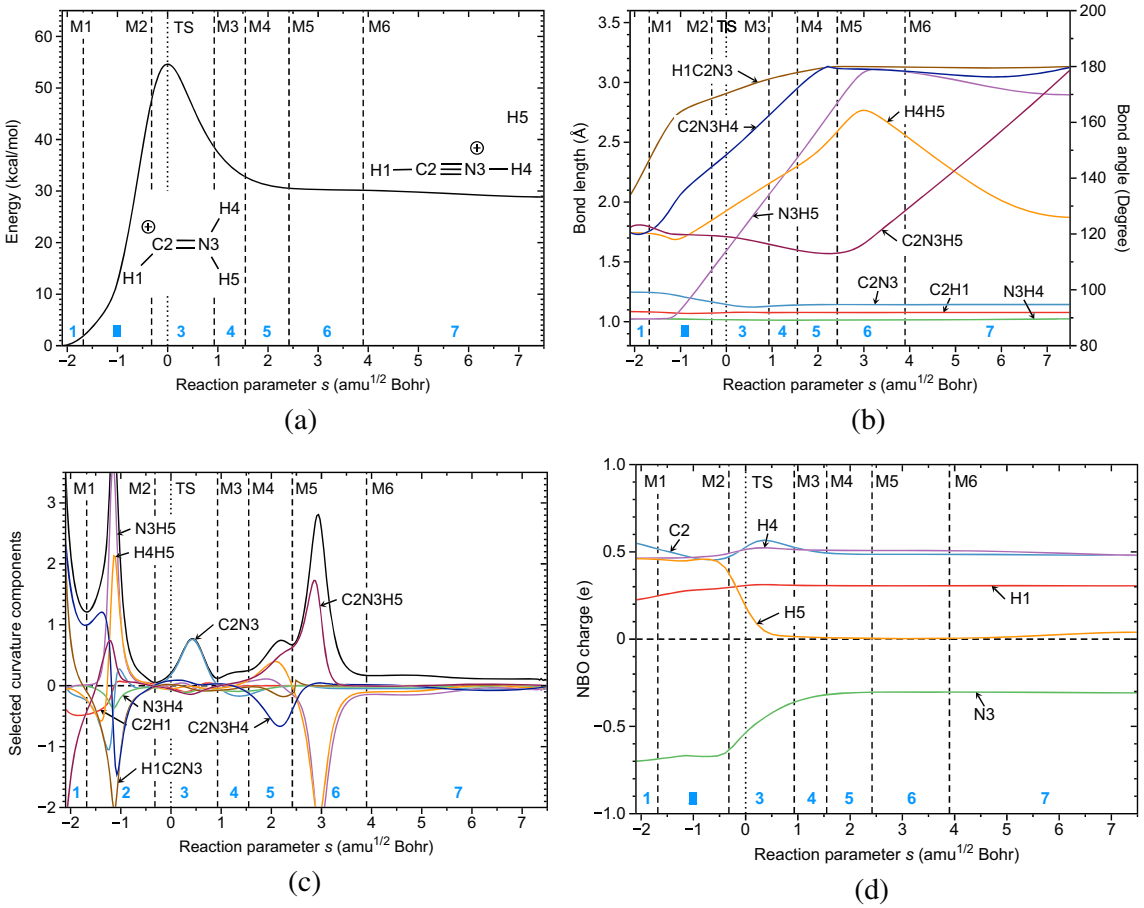

Fig. 5 Reaction **R4**; **a** energy profile; **b** changes in geometry parameters; **c** reaction path curvature profile (black solid line) and its decomposition into components; **d** changes in NBO charges as a function of the reaction path parameter s. Reaction phases are indicated by vertical dashed lines at curvature minima M1, M2, ..., Mn, and are labeled by blue numbers. The TS is indicated as a dotted line. MP2/aug-cc-pVTZ level of theory

the TS is dominated by the C2N3 contribution. In phase 6, the cleavage of the N3H5 bond is finalized with a large resisting contribution of the N3H5 and H4H5 components and supported by the C2N3H5 angle contribution. From there, one H5 roaming is taking place, which does not lead to any pronounced curvature. Figure 5d presents the changes of the NBO charges along s. Most pronounced is the transfer of charge from the nitrogen atom ($-0.7e$ at the start of the reaction, $-0.3e$ at the end) to the leaving H5 atom, which starts with a positive charge of $0.5e$ and becomes neutral at around s=1.0 amu$^{1/2}$ Bohr.

Reaction **R5** is the first reaction of *path 2* which leads to (7) in only two reaction steps. Starting from **3T**, the planar methylene amine cation **6** is formed via the loss of one methyl hydrogen atom (see Fig. 6a and reaction movie **SR5**, Supporting Information). As is revealed in Fig. 6b, the C3H4 bond starts to elongate at $s = -1.8$ amu$^{1/2}$ Bohr, then the C3H4 increases linearly over the remaining reaction until at s=2.0 amu$^{1/2}$ Bohr where the final value of 2.936 Å is reached. The N2C3 bond length decreases from 1.386 to 1.221 Å to transform from a single into a double bond. The most notable additional change is that of the H1N2C3H6 dihedral angle decreasing from 60° to 0° accompanied with the rehybridization of the carbon atom from sp^3 to sp^2 and the planarization of the molecule. Overall, most changes occur at the methyl group as shown in the reaction movie. Figure 6c shows the reaction path curvature profile and its decomposition. In contract to previous reactions, the curvature profile is relatively simple. There are 5 phases with two enhanced curvature peaks in phases 2 and 3, then a long phase 4 including **TS5** without noticeable curvature, i.e., without any major chemical events, and phase 5 with a pronounced curvature peak characterizing the finalization of this reaction. Phase 2 is characterized by H1N2C3 and N2C3H5 angle changes helping to get the C3H4 cleavage started, which occurs in phase 3, denoted by supporting C3H4 components the C3N2 bond changes its character, denoted by a supporting C3N2 component. C3H4 cleavage is completed in phase 5 characterized by a large resisting C3H4 contribution and a supporting N2C3H4 contribution.

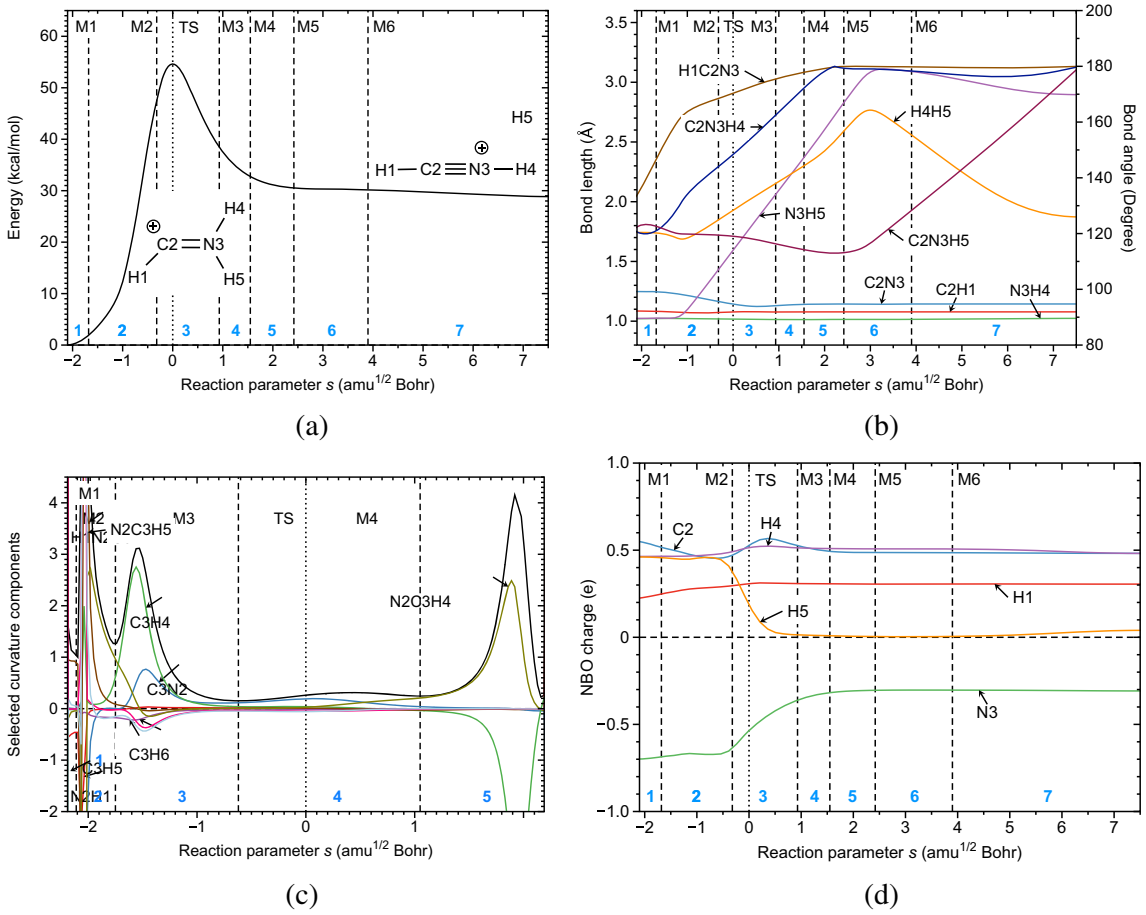

Fig. 6 Reaction **R5**; **a** energy profile; **b** changes in geometry parameters; **c** reaction path curvature profile (black solid line) and its decomposition into components; **d** changes in NBO charges as a function of the reaction path parameter s. Reaction phases are indicated by vertical dashed lines at curvature minima M1, M2, ..., Mn, and are labeled by blue numbers. The TS is indicated as a dotted line. MP2/aug-cc-pVTZ level of theory

In Fig. 6d, changes of the NBO charges along s are shown. As in reaction **R3**, negative charge is transferred from the carbon atom the nitrogen and to H4, which has to become neutral. However, compared to reaction **R3**, the resulting CN double bond in **6** is less polar with $0.09e$ on C3 and $-0.15e$ on N.

Reaction **R6** can be considered as a counterpart of reaction **R4**, both aiming at the formation of protonated hydrogen cyanide **7**; the difference is that in this reaction the methylene loses a hydrogen atom. The CH bond breakage is assisted by rotating the H1N2 and the C3H4 bonds into a linear arrangement which facilitates the cleavage of the C3H5 bond (see Fig. 7a and reaction movie **SR6**, Supporting Information). As shown in Fig. 7b, the H1N2C3 angle increases from 151° and the N2C3H4 angle from 120° in **6** to reach their final values of 180° at s=2.1 amu$^{1/2}$ Bohr. The C3H5 bond starts to elongate at $s = -1.2$ amu$^{1/2}$ Bohr, the C3H5 distance increases linearly until reaching the value of 3.1 Å at s=2.8 amu$^{1/2}$ Bohr, which is close to the final bond length. Interesting to note again is the assistance of a dihydrogen interaction. The H4H5 distance of 1.901 Å in **6** first decreases to a minimum value of 1.812 Å at $s = -1.0$ amu$^{1/2}$ Bohr, then increases to a maximum value of 2.944 Å at s=2.8 amu$^{1/2}$ Bohr and then decreasing again, showing the onset of a roaming motion which is however less pronounced than in reaction **R4**, as shown in the reaction movie, which is also reflected by a much smaller change of the N2C3H5 angle compared to the more drastic C2N3H5 angle changes in reaction **R4**. The reaction path curvature patterns of both reactions look quite similar; there are three distinct curvature peaks, two in the entrance and one in the exit channel. The big difference is that reaction **R6** has only six reaction phases and a shorter exit channel of 3.5 s units (see Fig. 7c) than **R4** because of the less pronounced roaming. Phase 1 is characterized by angle rotations, then in phase 2 the C3H5 bond starts to break, supported by H4H5 interactions leading to a large curvature peak. Another important contribution to this curvature peak is negative contribution of the H1N2C3 angle, resisting to become linear. The curvature peak in phase 3 shortly after

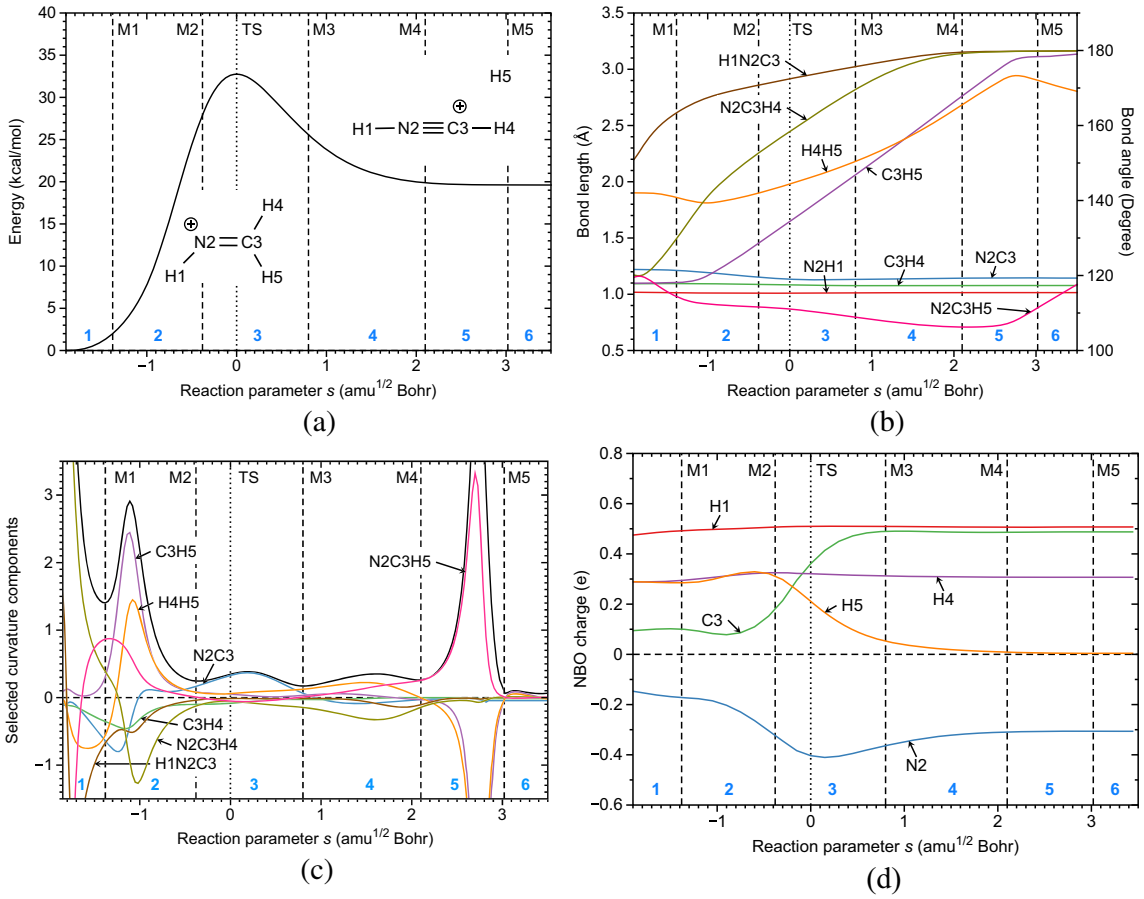

Fig. 7 Reaction **R6**; **a** energy profile; **b** changes in geometry parameters; **c** reaction path curvature profile (black solid line) and its decomposition into components; **d** changes in NBO charges as a function of the reaction path parameter s. Reaction phases are indicated by vertical dashed lines at curvature minima M1, M2, ..., Mn, and are labeled by blue numbers. The TS is indicated as a dotted line. MP2/aug-cc-pVTZ level of theory

the TS is dominated by the N2C3 contribution. In phase 6, the cleavage of the C3H5 bond is finalized with a large resisting contribution of the C3H5 and H4H5 components and supported by the N2C3H5 angle contribution. The short phase 6 describes the onset of a roaming motion of the leaving H5 atom. Figure 6d presents the changes of the NBO charges along s. In contrast to reaction **R4** here the neutralization of the leaving hydrogen atom H5 occurs via transfer of negative charge from the carbon atom.

Path 3 offers an attractive alternative for the formation of **R7** on the singlet PES via just one barrier-less reaction. As sketched in Fig. 1, after intersystem crossing of **3T** into **3S**, **7** is formed via the loss of H_2. The out of plane H5 and H6 methyl atoms (see Fig. 8a) leave simultaneously as depicted in reaction movie **SR7** (see Supporting Information) and combine to a hydrogen molecule. The process is initiated by the amino hydrogen atom, which moves towards the carbon atom helping to kick out H5 and H6 before swinging back into its final linear position in **R7**. As shown in Fig. 8b, both C3H5 and C3H6 distances change simultaneously, up to s=2.0 amu$^{1/2}$ Bohr more gradually, and thereafter in a steep linear fashion, until reaching their final value of 2.976 Å at s=8.4 amu$^{1/2}$ Bohr. At s=1.8 amu$^{1/2}$ Bohr, the H1N2C3 angle reaches a minimum of 114° before steadily increasing again reaching its final value of 180° at s=6.9 amu$^{1/2}$ Bohr. The C2C3 single bond of **3S** decreases smoothly from 1.386 to 1.144 Å, the triple bond distance of **7**, which is reached after s=5 amu$^{1/2}$ Bohr. The H1N2C3H5 and H1N2C3H6 dihedral angles of 60° approach a zero value upon leaving the newly formed H_2 as documented by the decreasing H5H6 distance which reaches the HH distance of 0.742 Å already at s=5.0 amu$^{1/2}$ Bohr before the final departure from the carbon atom. The reaction path curvature profile and its decomposition is shown in Fig. 8c. The reaction consists of seven distinct reaction phases with four distinct curvature peaks, in line with our previous findings that also reactions without a barrier possess detailed mechanistic features [99–101]. Phases 1 and 2 are dominated by a large negative H5H6 components resisting first the formation of H_2 which is balanced in phase 2 by a large supporting

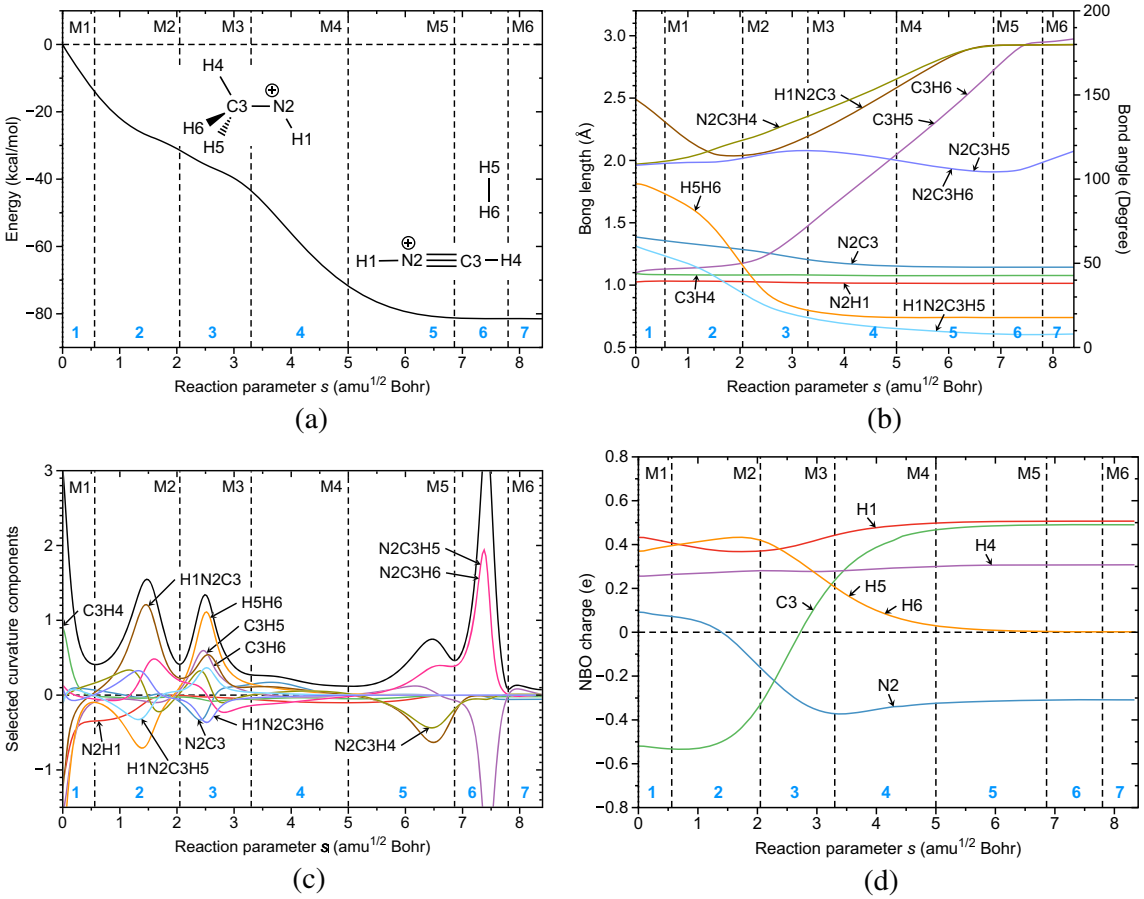

Fig. 8 Reaction **R7**; **a** energy profile; **b** changes in geometry parameters; **c** reaction path curvature profile (black solid line) and its decomposition into components; **d** changes in NBO charges as a function of the reaction path parameter s. Reaction phases are indicated by vertical dashed lines at curvature minima M1, M2, ..., Mn, and are labeled by blue numbers. MP2/aug-cc-pVTZ level of theory

contribution of the H1N2C3 angle. The actual cleavage of the C3H5 and C3H6 bonds and the combination of both leaving hydrogen atoms to form H_2 molecules start in a concerted fashion in phase 3 with supporting components. Interesting to note is that, as already predicted in Fig. 8b, the H_2 formation is completed at the end of phase 4, whereas the final CH bond cleavage occurs in phase 6, as denoted by the large resisting C3H5 and C3H6 components supported by large N2C3H5 and N2C3H6 contributions. The shoulder in phase 5 is characterized by adjustments of the N2C3H4 and H1N2C3 angles to become linear, which again is achieved before final CH bond cleavage. As denoted by the small N2C3 curvature components, the transformation from CN single to triple bond occurs mainly in phases 2 and 3 and is completed at the end of phase 4. Figure 8d shows the change of the NBO charges along s. There is a large transfer of negative charge from the carbon to the nitrogen atom as well as to the leaving hydrogen atoms which both have a zero charge in the H_2 molecule. C3 starts with a negative charge of $-0.5e$ and ends with a positive charge of $0.5e$, whereas N2 starts with a positive charge of $0.1e$ and negative charge of $-0.31e$ in **R7**.

Protonated hydrogen cyanide **7** formed in each of the three paths can recombine with molecular hydrogen and to the methylene amine cation **4S** which is planar in contrast to **4T**, and therefore can form a CN double bond; see Fig. 1. As shown in reaction movie **SR8** (see Supporting Information), a hydrogen molecule approaches **7** at the carbon end and causes the HCN and CNN bonds to bend into the opposite direction. In the first part of the reaction, H_2 is attached to the carbon atom resembling a reversion of reaction **R7**. In the second part, one of the H_2 hydrogen atoms migrates to the nitrogen forming **4S**. Obviously, this mechanism, which has been found, e.g., in transition metal catalysis [96] is more energy effective than starting via breaking the hydrogen bond in H_2, which costs more than 100 kcal/mol. As denoted by the small shoulder in energy profile at about $s = -2.0$ amu$^{1/2}$ Bohr (see Fig. 9a), reaction **R8** is at the onset for the two-step reaction mechanism. Figure 9b shows the geometric changes of reaction **R8** as a function

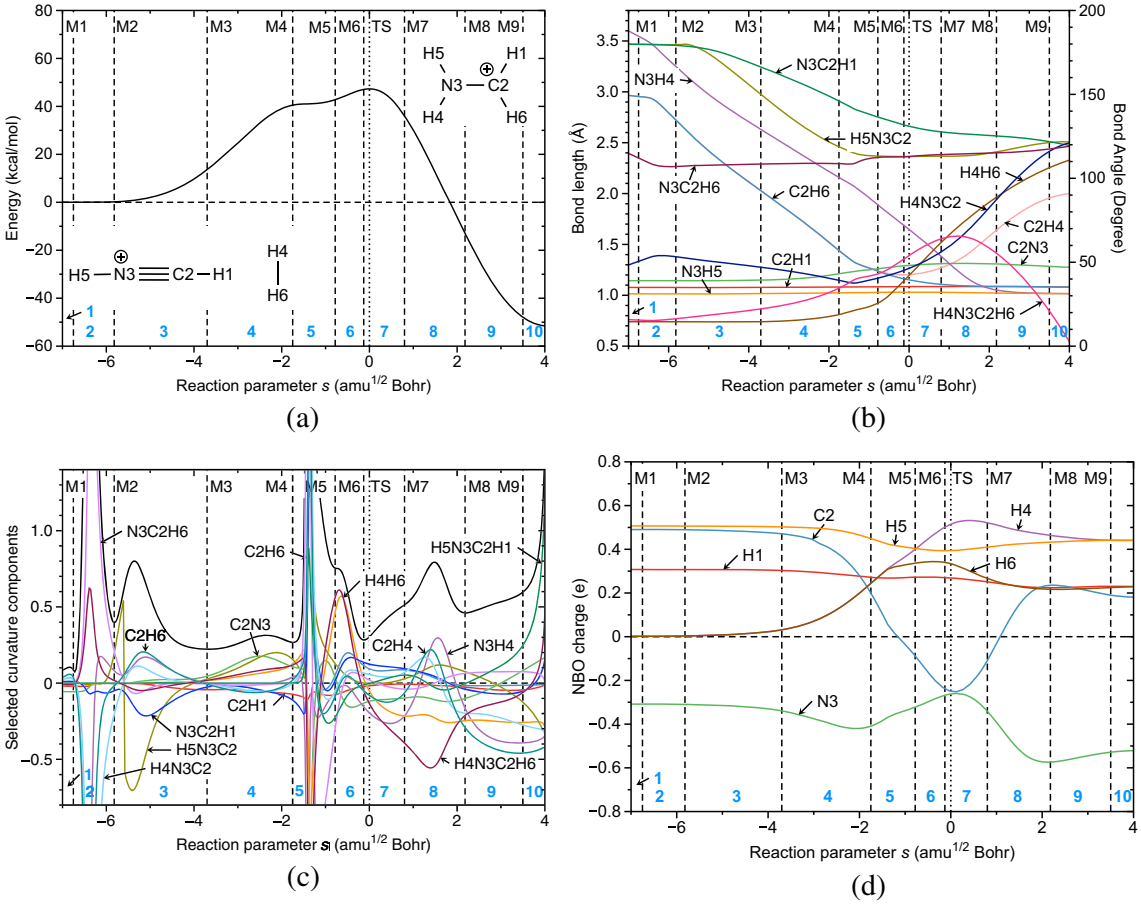

Fig. 9 Reaction **R8**; **a** energy profile; **b** changes in geometry parameters; **c** reaction path curvature profile (black solid line) and its decomposition into components; **d** changes in NBO charges as a function of the reaction path parameter s. Reaction phases are indicated by vertical dashed lines at curvature minima M1, M2, ..., Mn, and are labeled by blue numbers. The TS is indicated as a dotted line. MP2/aug-cc-pVTZ level of theory

of s. The H4H6 distance of 0.740 Å between the hydrogen atoms of the incoming H_2 molecule does not change for more than 3 s units, confirming that the H_2 molecule is captured by the carbon atom. At $s = -2.5$ amu$^{1/2}$ Bohr, the H4H6 distance slowly starts to increase; after $s = -0.8$ amu$^{1/2}$ Bohr, this distance is more pronounced as the split of H_2 and the migration of H4 to the nitrogen atom proceeds. At s=4.0 amu$^{1/2}$ Bohr, the final H4H6 distance of 2.331 Å is reached. The C2H4/C2H6 distance linearly decrease from 2.977 Å. At $s = -0.15$ amu$^{1/2}$ Bohr, the C2H6 distance further decreases to the value of 1.164 Å, whereas the C2H4 distance starts to increase from the value 1.201 Å in accordance with the starting H-migration. The N3H4 distance steadily decreases, until the final value of 1.016 Å is reached at s=3.8 amu$^{1/2}$ Bohr. Another interesting parameter is the H4N3C2H6 dihedral angle. Before reaching its final value of 0° in **4S**, the H4N3C2H6 dihedral angle adapts a maximum of 66° at s=1.1 amu$^{1/2}$ Bohr denoting that the migration of H4 occurs out the molecular plane. Further details about this complex reaction mechanism, including a quantification of the geometry discussion, can be gained by inspection of Fig. 9c showing the reaction path curvature profile and its decomposition. The reaction proceeds in 10 distinct phases, with **TS8** included in phase 7, i.e., several important chemical events occur before the TS. The large curvature peak in phase 2 is characterized by the adjustment of the incoming H_2 as reflected by supporting N3C2H6/N3C2H4, H4N3C2H6, and H4N3C2 resisting contributions. Phase 3 is dominated by the bending of **7**, resisting H5N3C2 and N3C2H1 components and a supporting C2H6/C2H4 component. The smaller curvature enhancement in phase 4 predominately results from changes in the CN bond and a start of H4H6 elongation. In phase 5, more drastic changes take place as reflected by the large curvature peak. The cleavage of the H4H6 bond and the migration of H4 start with a strongly resisting H4H6 component and supportive C2H6 and C2H4 components. Phase 6 is dominated by HH bond cleavage (supportive H4H6 component) and hydrogen migration (supportive H4N3C2H6 component). After the

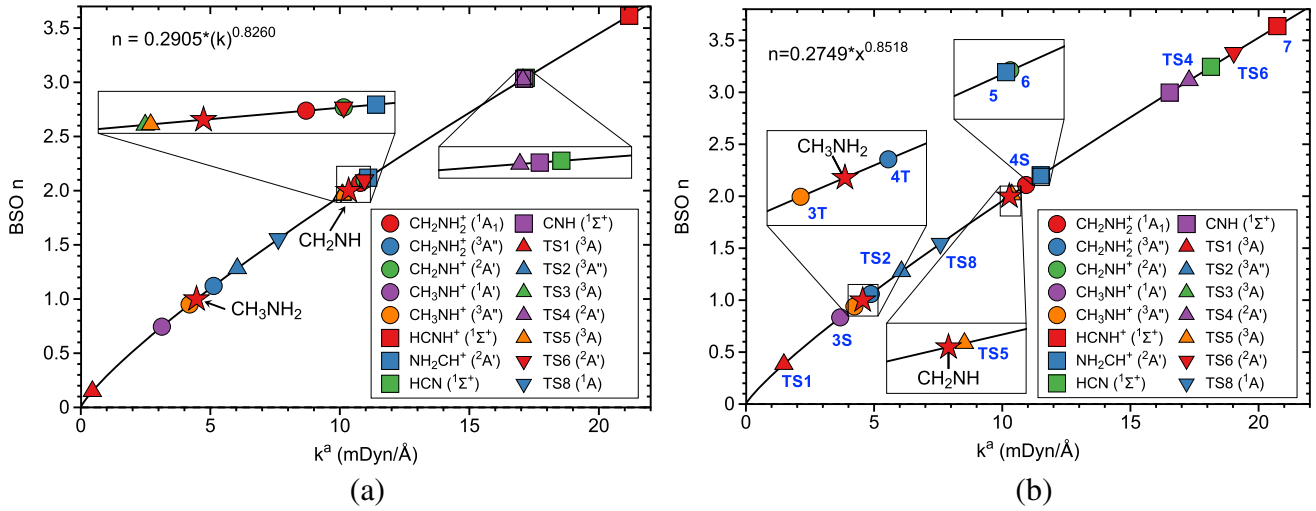

Fig. 10 Bond strength order BSO n as a function of the local mode force constant k^a for the CN bonds of all stationary points reactions **R1** – **R8** and some reference compounds (see legend). **a** CASPT2/aug-cc-pVTZ level of theory; **b** CCSD(T)/cc-pVDZ level of theory

TS, in phase 8, the final N3H4 distance is reached, denoted by large N3H4 and C2H4 components as well as the final C2H6 distance. There is still resistance to bring the molecule in its final planar form, i.e., large negative H4N3C2H6, which is then completed in phase 10 together with final bond angle adjustments. Figure 9d shows the NBO charges as a function of s. It is interesting to note changes of the NBO charges start only at the beginning of phase 4, where both hydrogens of the H_2 pick up positive charge predominately from C2 and to a lesser extent from N3. At $s = -1.4$ amu$^{1/2}$ Bohr, H4 starts to adapt more positive charge than H6 in accordance with its migration to the nitrogen atom. At the end of the reaction, the H4 and H5 hydrogens on N3 adapt a positive charge of $0.44e$ and the H1 and H6 hydrogens on carbon a positive charge of $0.23e$. Interesting to note is that shortly after the TS, both carbon and nitrogen are equally charged with $-0.26e$. After that point, negative charge is transferred back from C2 to N3 resulting in a polar CN double bond in **4S** with $0.18e$ on C2 and -0.52 on N3.

CN chemical bond analysis

The URVA analysis of chemical reactions **R1**–**R8** in this study was complemented by the assessment of the strength of all CN bonds formed during **R1**–**R8**. For this purpose, we calculated local mode force constants k^a with the CASPT2/aug-cc-pVTZ and CCSD(T)/cc-pVDZ model chemistries utilizing the LmodeA program [77].

In order to facilitate the discussion, local mode force constants k^a can be transformed into bond strength orders (BSO n) via a power relationship derived from the generalized Badger rule [82, 102]: $BSO\ n = A * (k^a)^B$; where the constants A and B are determined by two reference molecules with known BSO n and k^a values and the requirement that for a zero force constant k^a the corresponding BSO n value is also 0. We used in this work as a reference CH_3NH_2 with a CN bond order of 1 and CH_2NH with a CN bond order of 2. This led to constants $A = 0.291$ and $B = 0.826$ for CASPT2/aug-cc-pVTZ with k^a(C-N) of CH_3NH_2 = 4.467 mDyn/Å and k^a(C=N) of CH_2NH = 10.339 mDyn/Å and $A = 0.275$ and $B = 0.852$ for CCSD(T)/cc-pVDZ with k^a(C-N) of CH_3NH_2 = 4.555 mDyn/Å and k^a(C=N) of CH_2NH = 10.278 mDyn/Å.

The (BSO n, k^a) power relationship for all stationary points of reactions **R1**–**R8** and some reference compounds is shown in Fig. 10a for CASPT2/aug-cc-pVTZ and in Fig. 10b for CCSD(T)/cc-pVDZ. Bond distances R(CN), local mode force constants k^a(CN), and corresponding bond strength orders BSO n(CN) of all CN bonds in molecules **3**–**7**, TSs, and some reference compounds, calculated at the CASPT2/aug-cc-pVTZ and CCSD(T)/cc-pVTZ levels of theory are collected in Table 2. Noteworthy is the broad CN bond order spectrum observed in our study, ranging from almost 0 for the intermediate and **TS1** to 3.7 found for the protonated hydrogen cyanide **7** in accordance with previous work comparing the strength of the CN bond in **7** with that of the triple bond of double-protonated carbon monoxide [103]. In the following, we will limit the discussion to the CCSD(T)/cc-pVDZ results.

According to Fig. 1, we expect a very weak CN bond in both the intermediate formed from methane (**1**) and $N^+(^3P)$ as well as in the **TS1** which is confirmed by the BSO n values of 0.059 and 0.384, respectively (see Table 2 and Fig. 10b). Next follows a group of molecules with CN bonds in the single bond range, **3S** and **3T** and **4T** with BSO n values of 0.834, 0.939, and 1.059, respectively, followed

Table 2 Bond distances R(CN) in Å, local mode force constants k^a(CN) in mDyn/Å, and bond strength orders $BSO\ n$(CN) for molecules **3**–**7**, **TS1**–**TS6**, **TS8**, and some reference compounds, calculated at the CASPT2/aug-cc-pVTZ and CCSD(T)/cc-pVDZ levels of theory

	CASPT2/aug-cc-pVTZ			CCSD(T)/cc-pVDZ		
Molecule	R(CN)	k^a(CN)	BSO n(CN)	R(CN)	k^a(CN)	BSO n(CN)
vdW CH_3NH^+ (^{3}A")	1.825	0.257	0.095	2.027	0.163	0.059
3T CH_3NH^+ (^{3}A")	1.388	4.200	0.950	1.409	4.231	0.939
3S CH_3NH^+ ($^1A_1$)	1.388	3.129	0.745	1.409	3.678	0.834
4T CH_2NH2^+ (^{3}A")	1.392	5.127	1.121	1.413	4.872	1.059
4S CH_2NH2^+ ($^1A_1$)	1.280	10.789	2.072	1.290	10.930	2.108
5 $CHNH_2^+$ (^{2}A')	1.239	10.954	2.098	1.272	11.496	2.201
6 CH_2NH^+ (^{2}A')	1.261	11.096	2.120	1.252	11.520	2.205
7 $CHNH^+$ ($^1\Sigma^+$)	1.139	21.171	3.615	1.155	20.736	3.637
TS1 (^{3}A)	1.838	0.445	0.149	1.610	1.480	0.384
TS2 (^{3}A")	1.379	6.041	1.283	1.394	6.068	1.277
TS4 (^{2}A')	1.165	17.068	3.026	1.180	17.289	3.115
TS5 (^{3}A)	1.251	10.107	1.963	1.266	10.370	2.016
TS6 (^{2}A')	1.239	10.954	2.098	1.167	19.032	3.381
TS8 (^{1}A)	1.313	7.623	1.555	1.332	7.585	1.544
CH_3NH_2 ($^1A_1$)	1.465	4.467	1.000	1.473	4.555	1.000
CH_2NH ($^1A_1$)	1.275	10.339	2.000	1.289	10.278	2.000
CH_2NH_2 (^{2}A')	1.390	6.132	1.299	1.413	5.852	1.238
CHNH (^{2}A')	1.239	12.144	2.284	1.255	12.035	2.288
HCN ($^1\Sigma^+$)	1.165	17.175	3.042	1.175	18.140	3.246
CNH ($^1\Sigma^+$)	1.170	17.119	3.033	1.192	16.529	2.998

by **TS2** ($BSO\ n$= 1.277) which has a slightly shorter CN bond than found in **3T** and **4T** (see Table 2). **TS8** has with $BSO\ n$= 1.544 a somewhat weaker CN bond than expected from inspection of Fig. 1, which is the result of a widening of the CN bond caused by the migrating hydrogen atom, as underlined in the reaction movie **SR7** (see Supporting Information). The third group of CN bonds are in the CN double bond range, **TS5** with $BSO\ n$= 2.016, followed by **4S** where in contrast to **4T** the CN double can be formed, as reflected by a $BSO\ n$ value of 2.108. **5** and **6** with $BSO\ n$ values of 2.201 and 2.205 respectively also belong to this group. The final group contains molecules in the CN triple bond range. The first member of this group is **TS4** with a $BSO\ n$ value of 3.115 which is somewhat smaller than the $BSO\ n$ value of the CN bond in CNH, followed by **TS6** which has a somewhat stronger CN bond than the CN bond in the HCN molecule ($BSO\ n$ values of 3.381 and 3.246, respectively). **7** has with $BSO\ n$ = 3.637 the strongest CN bond found in this study. As discussed in a previous study [103], protonated hydrogen cyanide **7** belongs to the strongest bonds found in chemistry. In order to assess the effect of protonation on the bond strength, we calculated the CN bond strength in CHNH radical and CH_2NH_2 radical, the counterpart of **4**. In both cases, we observed a drastic decrease in the CN bond strength ($BSO\ n$ values of 2.288 compared to 3.637 in **7** and 1.238 compared to 2.108 in **4**, respectively, see Table 2), confirming the influence of protonation which strongly increases the electronegativity of the heavy atom involved.

Popular strategies to assess the strength of a chemical bond or weak chemical interaction often refer to bond distances [104–106]. However, a caveat is appropriate. A number of cases have been reported illustrating that a shorter bond is not always a stronger bond [107–109]. In the following, we discuss the situation for the CN bonds of this study using local mode force constants as a suitable assessment tool. In Fig. 7a, R(CN) and k^a(CN) values are correlated for CASPT2/aug-cc-pVTZ level of theory and in Fig. 7b for CCSD(T)/cc-pVDZ level of theory. For both model chemistries, similar trends are obtained and a good correlation between R(CN) and k^a(CN) with R^2=0.964 and R^2=0.967, respectively. We also see the separation into clusters as denoted in Fig. 7b, very weak and long CN bonds, one cluster in the CN single bond, one in the CN double bond, and one in the CN triple bond range, confirming that for the CN bonds investigated in this study the bond length-bond strength relationship is valid (Fig. 11).

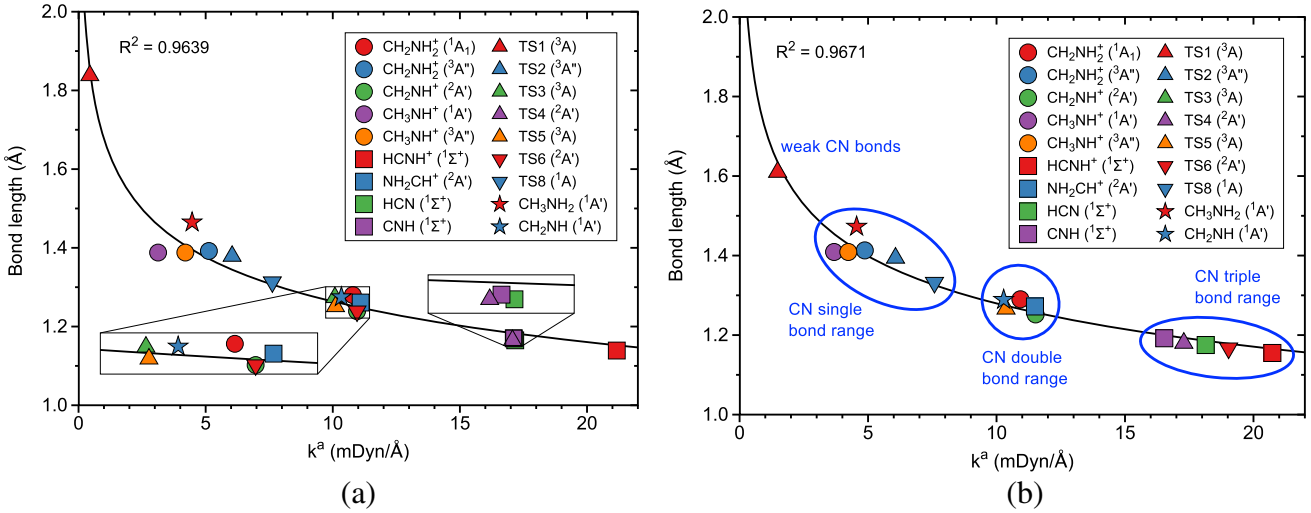

Fig. 11 Correlation between the CN bond length and local mode force constant k^a(CN) for all stationary points of reactions **R1**–**R8** and some reference compounds (see legend). **a** CASPT2/aug-cc-pVTZ level of theory; **b** CCSD(T)/cc-pVDZ level of theory

Conclusions and outlook

In this work, we investigated the formation of protonated hydrogen cyanide $HCNH^+$ (**7**) and methylene amine cation $CH_2NH_2{}^+$ (**4S**) from three different pathways which stem from the interaction between CH_4 (**1**) and $N^+(^3P)$ (**2**). Our URVA studies could provide a comprehensive overview on bond formation/cleavage processes relevant to the specific mechanism of eight reactions **R1**–**R8** that occur across the three pathways. In addition, we could explain the formation of $CH_2NH_2{}^+$ and the appearance of $HCNH^+$ and $CHNH_2^+$ along these paths. Although only smaller molecules are involved in these reactions including isomerization, hydrogen atom abstraction, and hydrogen molecule capture, we found a number of interesting features, such as *roaming* in reaction **R3** or the primary interaction of H_2 with the carbon atom in **7** in reaction **R8** followed by migrating of one of the H_2 hydrogen atoms to the nitrogen, which is more cost-effective than breaking the HH bond first; a feature often found in catalysis. In all cases, charge transfer between carbon and nitrogen could be identified as a driving force for the CN bond formation. Among the three possible pathways, the path via the singlet potential energy surface is the shortest, and therefore most favorable path for the formation of **7** and **4**. Several new specific insights emerged from our study.

1. For reactions **R1** and **R2**, no pronounced peaks were observed at the corresponding TS and significant chemical changes were seen to occur in both the entrance and exit channels revealing that major chemical events do not always take place at the TS.
2. From reaction **R4**, we observed the hydrogen atom H5 to orbit around the NH molecule rather than exiting on a straight pathway which resulted in a long exit channel due to this so-called *roaming* mechanism. Alongside roaming, **R4** involves the formation of a dihydrogen interaction during the reaction mechanism which is more commonly observed in transition metal catalysis. We note that the during the reaction **R6** there is similar assistance of such a dihydrogen interaction, where **R6** has one less phase and a much shorter exit channel in contrast to **4** due to a lesser extent of *roaming*.
3. *Path 3* was shown to be an appealing alternative for the formation of **R7** through one barrier-less reaction which involves intersystem crossing of the triplet state CH_3NH^+ into the singlet state CH_3NH^+ and a loss of H_2. Furthermore, **R7** was shown to consist of seven reaction phases and four curvature peaks demonstrating that reactions with a barrier also possess elaborate mechanistic features, where notably, at the end of phase 4 the H_2 formation is finished and the final CH bond cleavage takes place in phase 6 and the change from a C-N bond to a C≡C bond happens during phases 2 and 3 and is completed by phase 4.
4. Reaction **R8** is a complicated reaction mechanism that takes place across 10 distinct phases where the TS is within phase 7 with various important chemical events taking place prior to the TS, this reaction also features the formation of a dihydrogen interaction. An interesting feature of this reaction pertains to the start of phase 4 where the H_2 atoms (H4 and H6) collect positive charge mainly from C2 where H4 becomes more positive than H6 as it migrates towards the N atom.
5. As revealed by LMA, the CN bonds formed in reactions **R1**–**R8** cover a broad bond strength range from very weak ($BSO\ n$ values < 0.06) to very strong ($BSO\ n$ values > 3.5) with the CN bond in protonated hydrogen

cyanide $HCNH^+$ (**7**) identified as strongest of all molecules investigated in this work.

In summary, our study shows the large potential of both URVA and LMA to shed new light into these extraterrestrial reactions to help better understand prebiotic processes as well as develop guidelines for future investigations involving areas of complex interstellar chemistry. In particular, the formation of CN bonds as a precursor to the extraterrestrial formation of amino acids [110, 111] will be the focus of future investigations.

Supplementary Information The online version contains supplementary material available at https://doi.org/10.1007/s00894-021-04917-8.

Acknowledgements We thank SMU for generous computational resources.

Author contribution Conceptualization, E.K.; methodology, E.K. and M.F.; pURVA coding and testing, YT; validation, M.F. and N.B.; formal analysis, N.B. and M.F.; investigation, N.B, M.F. and A.D.; data curation, N.B. and M.F.; writing (original draft preparation), E.K.; writing (review and editing), E.K., AD, and M.F. visualization, N.B. and M.F.; supervision, E.K.; project administration, E.K.; funding acquisition, E.K. All the authors have read and agreed to the published version of the manuscript.

Funding This work was financially supported by the National Science Foundation, Grant 2102461.

Availability of data and materials All data generated or analyzed during this study are included in this published article. Additional information is provided in the Supporting Information which contains (i) the decomposition of the reaction path direction along the reaction parameter *s* for each reaction; (ii) reaction movies following the changes of the reaction complex along the reaction parameter *s* for each reaction; (iii) Cartesian coordinates of molecules **1**, **3**–**7**, transition states **TS1**–**TS6** and **TS8**, and some reference molecules.

Code availability The local mode analysis package LModeA can be obtained by the authors upon request.

Declarations

Conflict of interest The authors declare no competing interests.

References

1. Oberg KI, Bergin EA (2020) Astrochemistry and compositions of planetary. Systems. Phys. Rep.
2. Okada K, Sakimoto K, Takada Y, Schuessler HA (2020) A study of the translational temperature dependence of the reaction rate constant between CH_3CN and Ne^+ at low temperatures. J Chem Phys 153(12):124305
3. de Barros ALF, Bergantini A, Domaracka A, Rothard H, Boduch P, da Silveira EF (2020) Radiolysis of NH_3:CO ice mixtures - implications for solar system and interstellar ices. MNRAS 499(2):2162–2172
4. Dubois D, Carrasco N, Jovanovic L, Vettier L, Gautier T, Westlake J (2020) Positive ion chemistry in an N2-CH4 plasma discharge: key precursors to the growth of Titan Tholins. Icarus 338:113437
5. Tielens A (2013) The molecular universe. RMP 85(3):1021
6. Matson DL, Spilker LJ, Lebreton J-P (2003) The cassini/huygens mission to the saturnian system. The Cassini-Huygens Mission: 1–58
7. NASA: Cassini/Huygens Mission. NASA. See the website for a comprehensive overview
8. Werner MW, Roellig TL, Low FJ, Rieke GH, Rieke M, Hoffmann WF, Young E, Houck JR, Brandl B, Fazio GG, Hora JL, Gehrz RD, Helou G, Soifer BT, Stauffer J, Keene J, Eisenhardt P, Gallagher D, Gautier TN, Irace W, Lawrence CR, Simmons L, Van Cleve JE, Jura M, Wright EL, Cruikshank DP (2004) The spitzer space telescope mission. APIS 154(1):1–9
9. France K, Schindhelm E, Herczeg GJ, Brown A, Abgrall H, Alexander RD, Bergin EA, Brown JM, Linsky JL, Roueff E, et al. (2012) A hubble space telescope survey of H2 emission in the Circumstellar environments of young stars. ApJ 756(2):171
10. Gardner JP, Mather JC, Clampin M, Doyon R, Greenhouse MA, Hammel HB, Hutchings JB, Jakobsen P, Lilly SJ, Long KS, et al. (2006) The James Webb space telescope. Space Sci Rev 123(4):485–606
11. Fanson J, Bernstein R, Angeli G, Ashby D, Bigelow B, Brossus G, Bouchez A, Burgett W, Contos A, Demers R, et al. (2020) Overview and status of the giant magellan telescope project, vol 11445, p 114451. International Society for Optics and Photonics
12. Heazlewood BR, Softley TP (2021) Towards chemistry at absolute zero. Nat Rev Chem: 1–16
13. Cooke IR, Sims IR (2019) Experimental studies of gas-phase reactivity in relation to complex organic molecules in star-forming regions. ACS Earth Space Chem: 1109–1134
14. Smith IWM (2011) Laboratory astrochemistry: gas-phase processes. ARAA 49(1):29–66
15. Bourgalais J, Carrasco N, Vettier L, Gautier T, Blanchet V, Petit S, Descamps D, Fedorov N, Delos R, Gaudin J (2020) On an eUV atmospheric simulation chamber to study the photochemical processes of Titan's atmosphere. Sci 10(1):1–14
16. Bourgalais J, Carrasco N, Vettier L, Comby A, Descamps D, Petit S, Blanchet V, Gaudin J (2021) marty Bernard, aromatic formation promoted by ion-driven radical pathways in EUV photochemical experiments simulating Titan's atmospheric chemistry. J Phys Chem A 125:3159–3168
17. Sandford SA, Nuevo M, Bera PP, Lee TJ (2020) Prebiotic astrochemistry and the formation of molecules of astrobiological interest in interstellar clouds and protostellar disks. Chem Rev 120(11):4616–4659
18. Haupa KA, Ong W-S, Lee Y-P (2020) Hydrogen abstraction in astrochemistry: formation of CH_2CONH_2 in the reaction of H atom with acetamide (CH_3CONH_2) and photolysis of CH_2CONH_2 to form Ketene (CH_2CO) in solid para-hydrogen. Phys Chem Chem Phys 22(11):6192–6201
19. Noelle A, Vandaele AC, Martin-Torres J, Yuan C, Rajasekhar BN, Fahr A, Hartmann GK, Lary D, Lee Y-P, Limão-Vieira P., et al. (2020) UV/Vis+ photochemistry database: structure, content and applications. J Quant Spectrosc Radiat Transf 253: 107056
20. Lavvas P, Lellouch E, Strobel D, Gurwell M, Cheng A, Young L, Gladstone G (2021) A major ice component in Pluto's haze. Nat Astron 5(3):289–297
21. DIschia M, Manini P, Moracci M, Saladino R, Ball V, Thissen H, Evans RA, Puzzarini C, Barone V (2019) Astrochemistry and astrobiology: materials science in wonderland? Int J Mol Sci 20(17):4079
22. Thripati S, Ramabhadran RO (2021) Pathways for the formation of formamide, a prebiotic biomonomer: metal—ons in interstellar gas-phase chemistry. J Phys Chem A: 3457–3472

23. Vastel C, Loison JC, Wakelam V, Lefloch B (2019) Isocyanogen formation in the cold interstellar medium. Astron Astrophys: 91
24. Gavilan L, Broch L, Carrasco N, Fleury B, Vettier L (2017) Organic aerosols in the presence of $CO_2$2 in the Early Earth and Exoplanets: UV–Vis refractive indices of oxidized tholins. Astrophys J Letters: 5
25. Waite J, Young D, Cravens T, Coates A, Crary F, Magee B, Westlake J (2007) The process of Tholin formation in Titan's upper atmosphere. Science 316(5826):870–875
26. Cable ML, Hörst S. M., Hodyss R, Beauchamp PM, Smith MA, Willis PA (2012) Titan Tholins: simulating titan organic chemistry in the Cassini-Huygens era. Chem Rev 112(3):1882–1909
27. Neish CD, Somogyi A, Smith MA (2010) Titan's primordial soup: formation of amino acids via low-temperature hydrolysis of Tholins. Astrobiology 10(3):337–347
28. Dalton J, Cruikshank D, Stephan K, McCord T, Coustenis A, Carlson R, Coradini A (2010) Chemical composition of icy satellite surfaces. Space Sci Rev 153(1-4):113–154
29. Cravens TE, Robertson IP, Waite Jr. J. H., Yelle RV, Kasprzak WT, Keller CN, Ledvina SA, Niemann HB, Luhmann JG, McNutt RL, Ip W-H, De La Haye V, Mueller-Wodarg I, Wahlund J-E, Anicich VG, Vuitton V (2006) Composition of Titan's ionosphere. Geophys Res Lett 33(7):01003
30. Waite J, Lewis W, Kasprzak W, Anicich V, Block B, Cravens TE, Fletcher G, Ip W-H, Luhmann J, McNutt R, et al. (2004) The Cassini Ion and Neutral Mass Spectrometer (INMS) investigation. Space Sci Rev 114(1-4):113–231
31. Ennis C, Cable ML, Hodyss R, Maynard-Casely HE, Hydrocarbon Mixed (2020) Cyanide ice compositions for Titan's atmospheric aerosols a ternary-phase co-crystal predicted by density functional theory. ACS Earth and Space Chem 4(7):1195–1200
32. Kronrod V, Dunaeva A, Gudkova T, Kuskov O (2020) Matching of models of the internal structure and thermal regime of partially differentiated Titan with gravity field. Sol Syst Res 54(5):405–419
33. Markus CR, Thorwirth S, Asvany O, Schlemmer S (2019) High-resolution double resonance action spectroscopy in ion traps: vibrational and rotational fingerprints of $CH_2NH_2^+$. Phys Chem Chem Phys 21(48):26406–26412
34. Yuen CH, Ayouz MA, Balucani N, Ceccarelli C, Schneider F, Kokoouline V (2019) Dissociative recombination of $CH_2NH_2^+$: a crucial link with interstellar methanimine and Titan ammonia. MNRAS: 659–664
35. Markus CR, Thorwirth S, Asvany O, Schlemmer S (2019) High-resolution double resonance action spectroscopy in ion traps: vibrational and rotational fingerprints of $CH_2NH_2^+$. Phys Chem Chem Phys: 26406–26412
36. Richardson V, Alcaraz C, Geppert WD, Polasek M, Romanzin C, Sundelin D, Thissen R, Tosia P, Zabkae J, Ascenzia D (2021) The reactivity of methanimine radical cation (H_2CNH^+) and its isomer aminomethylene ($HCNH_2^+$) with Methane. Chem Phys Lett: 138611
37. Pei L, Farrar JM (2012) Ion imaging study of reaction dynamics in the $N^+ + CH_4$. System Int J Chem Phys 137(15):154312
38. Kraka E, Zou W, Tao Y, Freindorf M (2020) Exploring the mechanism of catalysis with the Unified Reaction Valley Approach (URVA) - a review. Catalysts 10:691
39. Kraka E, Zou W, Tao Y (2020) Decoding chemical information from vibrational spectroscopy data: local vibrational mode theory. WIREs: Comput Mol Sci 10:1480
40. Zou W, Sexton T, Kraka E, Freindorf M, Cremer D (2016) A new method for describing the mechanism of a chemical reaction based on the unified reaction valley approach. J Chem Theory Comput 12:650–663
41. Kraka E (2011) Reaction path hamiltonian and the unified reaction valley approach. WIREs Comput Mol Sci 1:531–556
42. Wilson EB, Decius JC, Cross PC (1955) Molecular vibrations. McGraw-Hill, New York
43. Califano S (1976) Vibrational states. Wiley, London
44. Herzberg G (1945) Molecular spectra and molecular structure, II. Infrared and Raman Spectra of Polyatomic Molecules. Van Nostrand, New York
45. Konkoli Z, Cremer D (1998) A new way of analyzing vibrational spectra. I. Derivation of adiabatic internal modes. Int J Quant Chem 67:1–9
46. Konkoli Z, Larsson JA, Cremer D (1998) A new way of analyzing vibrational spectra. II. Comparison of internal mode frequencies. Int J Quant Chem 67:11–27
47. Konkoli Z, Cremer D (1998) A new way of analyzing vibrational spectra. III. Characterization of normal vibrational modes in terms of internal vibrational modes. Int J Quant Chem 67: 29–40
48. Konkoli Z, Larsson JA, Cremer D (1998) A new way of analyzing vibrational spectra. IV. Application and testing of adiabatic modes within the concept of the characterization of normal modes. Int J Quant Chem 67:41–55
49. Cremer D, Larsson JA, Kraka E (1998) New developments in the analysis of vibrational spectra on the use of adiabatic internal vibrational modes. In: Parkanyi C (ed) Theoretical and computational chemistry. Elsevier, Amsterdam, pp 259–327
50. Zou W, Cremer D (2016) C_2 in a box: determining its Intrinsic Bond Strength for the $X^1\Sigma_g^+$ Ground State. Chem Eur J 22:4087–4097
51. Freindorf M, Kraka E (2020) Critical assessment of the FeC and CO bond strength in Carboxymyoglobin - A QM/MM local vibrational mode study. J Mol Model 26:281–128115
52. Yannacone S, Freindorf M, Tao Y, Zou W, Kraka E (2020) Local vibrational mode analysis of π-hole interactions between aryl donors and small molecule acceptors. Crystals 10:556–155625
53. Tao Y, Zhang L, Zou W, Kraka E (2020) Equilibrium geometries, adiabatic excitation energies and intrinsic C=C/C-H bond strengths of ethylene in lowest singlet excited states described by TDDFT. Symmetry 12:1545–1154513
54. Pekar KB, Lefton JB, McConville C, Burleson J, Sethio D, Kraka E, Runčevski T. (2020) Peritectic phase transition of benzene and acetonitrile into a cocrystal relevant to Titan, Saturn's moon. Chem Comm https://doi.org/10.1039/d0cc04999a
55. Tao Y, Zou W, Sethio D, Verma N, Qiu Y, Tian C, Cremer D, Kraka E (2019) In situ measure of intrinsic bond strength in crystalline structures: Local vibrational mode theory for periodic systems. J Chem Theory Comput 15:1761–1776
56. Delgado AAA, Humason A, Kalescky R, Freindorf M, Kraka E (2021) Exceptionally long covalent CC bonds - a local vibrational mode study. Molecules 26:950–195025
57. Beiranvand N, Freindorf M, Kraka E (2021) Hydrogen bonding in natural and unnatural base pairs - explored with vibrational spectroscopy. Molecules 26:2268–1226822
58. Head-Gordon M, Pople JA, Frisch MJ (1988) MP2 Energy evaluation by direct methods. Chem Phys Lett 153(6):503–506
59. Cremer D (2011) Møller-Plesset perturbation theory: from small molecule methods to methods for thousand of atoms. WIREs: Comput Mol Sci 1:509–530
60. Celani P, Werner H-J (2000) Multireference perturbation theory for large restricted and selected active space reference wave functions. J Chem Phys 112(13):5546–5557
61. Celani P, Werner H-J (2003) Analytical energy gradients for internally contracted second–order multireference perturbation theory. J Chem Phys 119(10):5044–5057

62. Győrffy W., Shiozaki T, Knizia G, Werner H-J (2013) Analytical energy gradients for second–order multireference perturbation theory using density fitting. J Chem Phys 138(10):104104
63. Dunning TH (1989) Gaussian basis sets for use in correlated molecular calculations. I. The atoms boron through neon and hydrogen. J Chem Phys 90(2):1007–1023
64. Bartlett RJ, Musiał M. (2007) Coupled-cluster theory in quantum chemistry. Rev Mod Phys 79(1):291–352
65. Christiansen O (2006) Coupled cluster theory with emphasis on selected new developments. Theor Chem Acc 116:106–123
66. Matthews DA, Cheng L, Harding ME, Lipparini F, Stopkowicz S, Jagau T-C, Szalay PG, Gauss J, Stanton J (2020) Coupled-cluster techniques for computational chemistry: the CFOUR program package. J Chem Phys 152(21):214108–121410836
67. Raghavachari K, Trucks GW, Pople JA, Head-Gordon M (1989) A fifth-order perturbation comparison of electron correlation theories. Chem Phys, Lett 157:479–483
68. Bartlett RJ, Watts JD, Kucharski SA, Noga J (1990) Non-iterative fifth-order triple and quadruple excitation energy corrections in correlated methods. Chem Phys, Lett 165:513–522
69. Stanton J (1997) Why CCSD(T) works: a different perspective. Chem Phys, Lett 281:130–134
70. Fukui K (1981) The path of chemical reactions - the IRC approach. Acc Chem Res 14(12):363–368
71. Hratchian HP, Kraka E (2013) Improved Predictor-Corrector Integrators For Evaluating Reaction Path Curvature. J Chem Theory Comput 9:1481–1488
72. Frisch MJ, Trucks GW, Schlegel HB, Scuseria GE, Robb MA, Cheeseman JR, Scalmani G, Barone V, Petersson GA, Nakatsuji H, Li X, Caricato M, Marenich AV, Bloino J, Janesko BG, Gomperts R, Mennucci B, Hratchian HP, Ortiz JV, Izmaylov AF, Sonnenberg JL, Williams-Young D, Ding F, Lipparini F, Egidi F, Goings J, Peng B, Petrone A, Henderson T, Ranasinghe D, Zakrzewski VG, Gao J, Rega N, Zheng G, Liang W, Hada M, Ehara M, Toyota K, Fukuda R, Hasegawa J, Ishida M, Nakajima T, Honda Y, Kitao O, Nakai H, Vreven T, Throssell K, Montgomery Jr JA, Peralta JE, Ogliaro F, Bearpark MJ, Heyd JJ, Brothers EN, Kudin KN, Staroverov VN, Keith TA, Kobayashi R, Normand J, Raghavachari K, Rendell AP, Burant JC, Iyengar SS, Tomasi J, Cossi M, Millam JM, Klene M, Adamo C, Cammi R, Ochterski JW, Martin RL, Morokuma K, Farkas O, Foresman JB, Fox DJ (2016) Gaussian 16. Gaussian Inc Wallingford CT
73. Werner H-J, Knowles PJ, Knizia G, Manby FR, Schütz M., Celani P, Györffy W., Kats D, Korona T, Lindh R, Mitrushenkov A, Rauhut G, Shamasundar KR, Adler TB, Amos RD, Bennie SJ, Bernhardsson A, Berning A, Cooper DL, Deegan MJO, Dobbyn AJ, Eckert F, Goll E, Hampel C, Hesselmann A, Hetzer G, Hrenar T, Jansen G, Köppl C, Lee SJR, Liu Y, Lloyd AW, Ma Q, Mata RA, May AJ, McNicholas SJ, Meyer W, Miller III TF, Mura ME, Nicklass A, O'Neill DP, Palmieri P, Peng D, Pflüger K., Pitzer R, Reiher M, Shiozaki T, Stoll H, Stone AJ, Tarroni R, Thorsteinsson T, Wang M, Welborn M MOLPRO, version 2021.1, A Package of ab initio Programs, University of Stuttgart, Pfaffenwaldring 55 D-70569 Stuttgart, Germany. https://www.molpro.net
74. Werner H-J, Knowles PJ, Manby FR, Black JA, Doll K, Heßelmann A., Kats D, Köhn A., Korona T, Kreplin DA, Ma Q, Miller TF, Mitrushchenkov A, Peterson KA, Polyak I, Rauhut G, Sibaev M (2020) The Molpro quantum chemistry package. J Chem Phys 152(14):144107
75. Werner H-J, Knowles PJ, Knizia G, Manby FR, Schütz M (2012) Molpro: a general–purpose quantum chemistry program package. Mol Sci 2(2):242–253
76. Tao Y, Zou W, Freindorf M, Cremer D, Kraka E (2020) pURVA. Southern Methodist University: Dallas, TX USA
77. Zou W, Tao Y, Freindorf M, Makoś MZ, Verma N, Kraka E (2020) Local Vibrational mode analysis: LModeA. Computational and theoretical chemistry group (CATCO), Southern Methodist University: Dallas, TX USA
78. Reed AE, Curtiss LA, Weinhold F (1988) Intermolecular interactions from a natural bond orbital, donor-acceptor viewpoint. Chem Rev 88:899–926
79. Weinhold F, Landis CR (2003) Valency and bonding: a natural bond orbital donor-acceptor perspective. Cambridge University Press, Cambridge
80. Glendening ED, Badenhoop JK, Reed AE, Carpenter JE, Bohmann JA, Morales CM, Landis CR, Weinhold F. (2013) NBO6
81. Park JW, Al-Saadon R, MacLeod MK, Shiozaki T, Vlaisavljevich B (2020) Multireference electron correlation methods: journeys along potential energy surfaces. Chem Rev 120:5878–5909
82. Cremer D, Kraka E (2010) From molecular vibrations to bonding, chemical reactions, and reaction mechanism. Curr Org Chem 14:1524–1560
83. Kalescky R, Kraka E, Cremer D (2014) Are carbon-halogen double and triple bonds possible? Int J Quant Chem 114:1060–1072
84. Kalescky R, Zou W, Kraka E, Cremer D (2014) Quantitative assessment of the multiplicity of carbon-halogen bonds: carbenium and halonium ions with F, Cl, Br, and I. J Phys Chem A 118:1948–1963
85. Oliveira V, Kraka E, Cremer D (2016) Quantitative assessment of halogen bonding utilizing vibrational spectroscopy. Inorg Chem 56:488–502
86. Setiawan D, Sethio D, Cremer D, Kraka E (2018) From strong to weak NF bonds: on the design of a new class of fluorinating agents. Phys Chem Chem Phys 20:23913–23927
87. Sethio D, Oliveira V, Kraka E (2018) Quantitative assessment of tetrel bonding utilizing vibrational spectroscopy. Molecules 23:2763
88. Sexton TM, Freindorf M, Kraka E, Cremer D (2016) A reaction valley investigation of the cycloaddition of 1,3-Dipoles with the dipolarophiles ethene and acetylene: solution of a mechanistic puzzle. J Phys Chem A 120:8400–8418
89. Reis MC, López C. S., Kraka E, Cremer D, Faza ON (2016) Rational design in catalysis: a mechanistic study of β-hydride eliminations in Gold(I) and Gold(III) complexes based on features of the reaction valley. Inorg Chem 55:8636–8645
90. Sexton T, Kraka E, Cremer D (2016) Extraordinary mechanism of the diels-alder reaction: investigation of stereochemistry, charge transfer, charge polarization, and biradicaloid formation. J Phys Chem A 120:1097–1111
91. Makoś MZ, Freindorf M, Tao Y, Kraka E (2021) Theoretical insights into [NHC]Au(I) catalyzed hydroalkoxylation of allenes: a unified reaction valley approach study. J Org Chem 86:5714–5726
92. Freindorf M, Cremer D, Kraka E (2017) Gold(I)-assisted catalysis - a comprehensive view on the [3,3]-Sigmatropic rearrangement of allyl acetate. Mol Phys 116:611–630
93. Bowman JM, Houston PL (2017) Theories and simulations of roaming. Chem Soc Rev 46:7615–7624
94. Quinn MS, Nauta K, Jordan MJT, Bowman JM, Houston PL, Kable SH (2020) Rotational resonances in the H_2CO roaming reaction are revealed by detailed correlations. Science 369:1592–1596
95. Endo T, Neville SP, Wanie V, Beaulieu S, Qu C, Deschamps J, Lassonde P, Schmidt BE, Fujise H, Fushitani M, Hishikawa A, Houston PL, Bowman JM, Schuurman MS, Legare F, Ibrahim H (2020) Capturing roaming molecular fragments in real time. Science 370:1072–1077

96. Makoś M. Z., Freindorf M, Sethio D, Kraka E (2019) New insights into Fe–H_2 and Fe–H^- Bonding of a [NiFe] Hydrogenase Mimic – a local vibrational mode study. Theor Chem Acc 138:76
97. Bakhmutov VI (2008) Dihydrogen bonds - principles, experiments, and applications. Wiley Ingterscience, New York
98. Karas LJ, Wu C-H, Das R, Wu JI-C (2020) Hydrogen bond design principles. WIREs Comput Mol Sci 10:1477–1147715
99. Kraka E, Joo H, Cremer D (2010) A stunning example for a spontaneous reaction with a complex mechanism: the vinylidene-acetylene cycloaddition reaction. Mol Phys 108:2667–2685
100. Joo H, Kraka E, Quapp W, Cremer D (2007) The mechanism of a barrierless reaction: hidden transition state and hidden intermediates in the reaction of methylene with ethene. Mol Phys 105:2697–2717
101. Quapp W, Kraka E, Cremer D (2007) Finding the transition state of quasi-barrierless reactions by a growing string method for newton trajectories: application to the dissociation of methylenecyclopropene and cyclopropane. J Chem Phys A 111:11287–11293
102. Kraka E, Larsson JA, Cremer D (2010) Generalization of the badger rule based on the use of adiabatic vibrational modes. In: Grunenberg J (ed) Computational spectroscopy. Wiley, New York, pp 105–149
103. Kalescky R, Kraka E, Cremer D (2013) Identification of the strongest bonds in chemistry. J Phys Chem A 117:8981–8995
104. Zhao L, Pan S, Holzmann N, Schwerdtfeger P, Frenking G (2019) Chemical bonding and bonding models of main-group compounds. Chem Rev 119:8781–8845
105. Gavezzotti A (2016) Comparing the strength of covalent bonds, intermolecular hydrogen bonds and other intermolecular interactions for organic molecules: x-ray diffraction data and quantum chemical calculations. New J Chem 40:6848–6853
106. Kraka E, Cremer D (2009) Characterization of CF bonds with multiple-bond character: bond lengths, stretching force constants, and bond dissociation energies. ChemPhysChem 10:686–698
107. Kraka E, Cremer D (2012) Weaker Bonds with shorter bond lengths. Rev Proc Quim: 39–42
108. Kraka E, Setiawan D, Cremer D (2015) Re-evaluation of the bond length-bond strength rule: the stronger bond is not always the shorter bond. J Comp Chem 37:130–142
109. Kaupp M, Danovich D, Shaik S (2017) Chemistry is about energy and its changes: a critique of bond-length/bond-strength correlations. Coord Chem Rev 344:355–362
110. Takeuchi Y, Furukawa Y, Kobayashi T, Sekine T, Terada N, Kakegawa T (2020) Impact-induced amino acid formation on Hadean Earth and Noachian Mars. Sci Rep 10:9220–192 207
111. Puzzarini C, Salta Z, Tasinato N, Lupi J, Cavallotti C, Barone V (2020) A twist on the reaction of the CN radical with methylamine in the interstellar medium: new hints from a state-of-the-art quantum-chemical study. MNRAS 496:4298–4310